



HAL
open science

Ice front blocking of ocean heat transport to an Antarctic ice shelf

Anna K. Wåhlin, Nadine Steiger, Elin Darelius-Chiche, Karen M. Assmann,
Mirjam S. Glessmer, Ho Kyung Ha, Laura Herraiz-Borreguero, Céline Heuzé,
Adrian Jenkins, Tae-Wan Kim, et al.

► **To cite this version:**

Anna K. Wåhlin, Nadine Steiger, Elin Darelius-Chiche, Karen M. Assmann, Mirjam S. Glessmer, et al.. Ice front blocking of ocean heat transport to an Antarctic ice shelf. *Nature*, 2020, 578 (7796), pp.568-571. 10.1038/s41586-020-2014-5 . hal-02495496

HAL Id: hal-02495496

<https://hal.science/hal-02495496>

Submitted on 1 Sep 2020

HAL is a multi-disciplinary open access archive for the deposit and dissemination of scientific research documents, whether they are published or not. The documents may come from teaching and research institutions in France or abroad, or from public or private research centers.

L'archive ouverte pluridisciplinaire **HAL**, est destinée au dépôt et à la diffusion de documents scientifiques de niveau recherche, publiés ou non, émanant des établissements d'enseignement et de recherche français ou étrangers, des laboratoires publics ou privés.

1 **Ice front blocking of ocean heat transport to an Antarctic ice shelf**

2 Wåhlin, A.K*., Steiger, N., Darelius, E., Assmann, K.M., Glessmer, M.S., Ha, H.K., Herraiz-
3 Borreguero, L., Heuzé, C., Jenkins, A., Kim, T.W., Mazur, A.K., Sommeria, J., Viboud, S.

4 Correspondence to: awahlin@gu.se

5

6

7 **Introductory paragraph:**

8 Mass loss from the Antarctic Ice Sheet to the ocean has increased in recent decades, largely
9 because the thinning of its floating ice shelves has allowed the outflow of grounded ice to
10 accelerate^{1,2}. Enhanced basal melting of the ice shelves is thought to be the ultimate driver of
11 change^{2,3}, motivating a recent focus on the processes that control ocean heat transport onto
12 and across the seabed of the Antarctic continental shelf towards the ice⁴⁻⁶. However, the
13 shoreward heat flux typically far exceeds that required to match observed melt rates^{2,7,8},
14 suggesting other critical controls. Here we show that the depth-independent (barotropic)
15 component of the flow towards an ice shelf is blocked by the dramatic step shape of the ice
16 front, and that only the depth-varying (baroclinic) component, typically much smaller, can
17 enter the sub-ice cavity. Our results arise from direct observations of the Getz Ice Shelf
18 system and laboratory experiments on a rotating platform. A similar blocking of the
19 barotropic component may occur in other areas with comparable ice-bathymetry
20 configurations, which may explain why changes in the density structure of the water column
21 have been found to be a better indicator of basal melt rate variability than the heat transported
22 onto the continental shelf⁹. Representing the step topography of the ice front accurately in
23 models is thus important for simulating the ocean heat fluxes and induced melt rates.

24

25 **Main text:**

26 The fate of the Antarctic Ice Sheet is the greatest remaining uncertainty when predicting
27 future sea level¹⁰. Estimates of its contribution to global sea-level rise range from none to a
28 catastrophic > 5 cm/year¹⁰⁻¹² (4 m by the year 2100). The ice sheet drains into the ocean
29 where it terminates in floating ice shelves, overlying vast sub-ice cavities. These buttress the
30 flow of the ice sheet, regulating the speed at which it flows into the ocean¹³. Rapid thinning of
31 ice shelves in coastal regions with warm ocean water on the continental shelf is accelerating
32 the outflow from the ice sheet^{1,2}. The perceived reason - although rarely observed directly¹⁴ -
33 is that ocean currents deliver more warm water to the ice shelf cavities, causing increased
34 basal melt. These currents originate in a reservoir of warm and salty water, known as
35 Circumpolar Deep Water (CDW)¹⁵, residing at 300-1000 m depth in the Southern Ocean.
36 Substantial amounts of dense CDW are carried onto the continental shelf by various
37 mechanisms^{4-7,16}, but only a fraction of this is needed to explain observed basal melt rates¹⁷.
38 The CDW flows southward in deep troughs that crosscut the continental shelf^{4,18-21}. The
39 currents are steered by the bathymetry and move with shallower water to the left of the flow
40 direction²²⁻²⁴ so southward transport occurs along the eastern, and northward on western,

41 flanks of the troughs^{19,25}. The flow is a combination of barotropic (vertically constant, wind-
42 driven^{26,27}) and baroclinic (vertically varying, density-driven) currents. Although the
43 barotropic velocities often dominate^{27,28}, most of the heat is contained in the warm dense
44 water below the thermocline where the baroclinic component typically enhances the flow.

45 In order to enter the ice shelf cavity the currents must pass the ice front - a wall of ice
46 protruding from the surface to depths of 250 – 500 m. This front imposes an abrupt change in
47 the thickness of the water column, potentially disrupting the topographically steered flow
48 towards it²⁹. Logistical challenges generally prevent observations near the ice front, and
49 estimates of oceanic heat transport towards the ice shelves are based on moorings placed at a
50 'safe' distance (at least a few km) away from the ice front.

51 To examine the effect of the ice front on the along-trough current, three moorings equipped
52 with velocity profilers and loggers for temperature, salinity, and pressure were placed in a
53 deep trough leading to Getz Ice Shelf (Fig. 1). Two of the moorings were positioned 14 km
54 and 11 km away from the ice front at depths of 600 and 700 m respectively, while the third
55 was placed 700-800 m from the front at 600 m depth. The ice front draft is 250-300 m³⁰, and
56 its position was constant during the two years of measurements (Fig. 1).

57 Feather-plots of the average velocity at various depths for the three moorings (Fig. 1,
58 Methods, full time series in Extended Data Figs 1-3) show a persistent current up to 30 cm/s
59 directed towards the ice shelf, parallel to the local bathymetry⁸. The velocity at the near-front
60 mooring was less than one third of those in the channel and deflected westward by up to 45°.

61 Separating the currents into barotropic and baroclinic components (Fig. 2, Methods, Extended
62 Data Figs 4-5) reveals that while GW1 and GW2 had significant barotropic along-slope flow
63 (7.5 and 10 cm/s) with a baroclinic amplification in the warm bottom layer, the velocity at
64 GW3 had a comparatively small barotropic component (0.1 cm/s) and was dominated by the
65 baroclinic flow in the warm bottom layer. The direction of the baroclinic flow at GW3 is into
66 the ice shelf cavity, i.e. parallel to the local topography and orthogonal to the ice front. It
67 should be noted however that the bathymetry underneath the ice shelf has not yet been
68 surveyed³¹. In the un-surveyed areas south of mooring GW3 the compilation used in Fig. 1 is
69 based on gravity inversions associated with high uncertainty³¹. If there are underwater
70 features such as submarine ridges and seamounts present underneath the ice shelf these might
71 redirect the flow.

72 The strong correlation between the velocity at GW3 and the baroclinic velocities at GW1 and
73 GW2 (Fig. 2 and Table 1, dark blue fields), indicates that the baroclinic current component at
74 GW1 and GW2 is continuing to GW3. The barotropic component however has no significant

75 correlation to the GW3 velocity, suggesting that it is diverted along the ice shelf front before
76 it reaches GW3 (Fig. 1, Fig. 2). This is further evidenced by the high correlation between
77 bottom temperature/density anomalies at GW2 and GW3 (both at the 600 m isobaths, Table 1,
78 dark blue field). The barotropic component of the flow carries about 70% of the total heat
79 transport (Extended Data Table 1, Extended Data Figure 6, Methods) at GW1 and GW2,
80 similar to values on the central Amundsen Shelf²⁷, while at GW3 it carries only 3-10% (based
81 on the more realistic methods (i) or (ii) for estimating barotropic velocity, see Methods). The
82 heat transport is dominated by the mean flow rather than the fluctuations assessed in Table 1
83 (Extended Data Table 1).

84 The observed behavior of the velocity components at the ice front can be explained by
85 geostrophic ocean dynamics^{22,29}. Geostrophic currents are non-divergent and therefore flow
86 parallel to lines of constant water column thickness, or, in the open ocean, lines of constant
87 depth^{22,24}. This is the reason why the currents in the deep troughs are so strongly steered by
88 the (comparatively gentle) topography. However, where a floating ice shelf with a
89 considerable draft overlies the ocean, the water column thickness is no longer equal to the
90 depth. Applied to the present setting this means that barotropic currents approaching the ice
91 front along depth contours will be diverted due to the change in water column thickness
92 (Methods) and may be blocked entirely without reaching the ice shelf cavity²⁹. Baroclinic
93 flow, on the other hand, can move along depth contours into the ice shelf cavity, provided the
94 thermocline is deeper than the ice shelf draft.

95 In order to explore this phenomenon in a controlled environment, experiments were
96 conducted in the 13-m diameter rotating Coriolis platform in Grenoble, France. A simplified
97 bathymetry - a v-shaped trough - was placed in a 90-cm deep tank filled with fresh water (Fig.
98 3). A source was placed on the right flank (facing North) of the trough, pumping fresh water
99 to set up a barotropic current, or saline (denser) water for a baroclinic bottom current. At the
100 far end of the trough a plexiglass ice shelf with adjustable draft was placed. A detailed
101 description of the experimental setup is presented in Methods.

102 The experimental results agree qualitatively with the geostrophic dynamics outlined above.
103 The current followed the trough flank towards the ice shelf, and away from it on the opposite
104 side, in similarity with observations^{19,25} (Fig. 4). Placing an ice shelf with near-zero draft on
105 top of the trough (Fig. 4A) had no visible impact on the circulation. However, a sloping ice
106 shelf with zero draft at the front and 30 cm at the back (Fig. 4B) caused the barotropic flow to
107 change direction and follow lines of constant water thickness into the ice shelf cavity. A
108 horizontal ice shelf with 30 cm draft (Fig. 4C) blocked the current from entering the cavity.

109 The baroclinic currents (Extended Data Fig. 9) continued mostly unaffected into the ice shelf
110 cavity for all ice shelf drafts and shapes.

111 The observational and experimental results presented here enhance our understanding of how
112 changes in oceanic heat transport on the continental shelf can impact basal melt. Barotropic
113 flow is blocked, either partially or entirely, depending on the ice front geometry, from
114 entering the cavity. Changes in the water temperature and/or baroclinic flow, on the other
115 hand, will change the amount of heat that flows into the cavity. How much of it is ultimately
116 used for basal melting depends on the cavity efficiency³². The results explain why changes in
117 the thickness of the warm water layer seem to be a more reliable indicator of melt rate
118 variability than e.g. ocean transports across the shelf break. Changes in the vertical structure
119 of the water column is a better diagnostic of the critical baroclinic heat transport.

120 Since flows toward ice shelf cavities nearly always have a substantial barotropic
121 component^{8,26,27,33}, the findings have broad implications for calculations of ocean heat
122 transport to ice shelf cavities. For example, the measured heat transport along the Siple
123 Trough is 2.27-2.8 TW (Extended Data Table 1) - sufficient to melt about 250-300 Gt/yr ice
124 and twice the total basal melt, 136 Gt/yr, that the entire Getz ice shelf experiences¹⁷.
125 However, due to the abrupt front shape only one sixth (0.47 TW) of the heat that flows past
126 GW1-2 enters the cavity. The results indicate that the floating ice shelves not only give back-
127 stress, mechanically slowing down the inland ice sheet¹³, but that they also protect the
128 vulnerable grounded ice by blocking a large portion of the warm ocean currents from reaching
129 the cavity. The thickness and shape of the ice front may provide a critical and evolving
130 control that needs to be incorporated accurately in models: Were an ice front to thin
131 substantially, or to retreat back (or advance) to a region with larger underwater features
132 steering the warm currents towards the cavity, then the heat flux to the ice sheet could change
133 dramatically. Rare observations from inside the cavity^{14,34} are needed to determine e.g. how
134 much of the heat transport that eventually reaches the vulnerable grounding zones.

135

136 **References:**

- 137 1. Shepherd, A., Fricker, H. A. & Farrell, S. L. Trends and connections across the
138 Antarctic cryosphere. *Nature* **558**, 223–232 (2018).
- 139 2. Pritchard, H. D. *et al.* Antarctic ice-sheet loss driven by basal melting of ice shelves.
140 *Nature* **484**, 502–505 (2012).
- 141 3. Liu, Y. *et al.* Ocean-driven thinning enhances iceberg calving and retreat of Antarctic

- 142 ice shelves. *Proc. Natl. Acad. Sci. U. S. A.* **112**, 3263–8 (2015).
- 143 4. Thoma, M., Jenkins, A., Holland, D. & Jacobs, S. Modelling Circumpolar Deep Water
144 intrusions on the Amundsen Sea continental shelf , Antarctica. *Geophys. Res. Lett.* **35**,
145 1–6 (2008).
- 146 5. Wåhlin, A. K. *et al.* Some Implications of Ekman Layer Dynamics for Cross-Shelf
147 Exchange in the Amundsen Sea. *J. Phys. Oceanogr.* **42**, 1461–1474 (2012).
- 148 6. Darelius, E., Fer, I. & Nicholls, K. W. Observed vulnerability of Filchner-Ronne Ice
149 Shelf to wind-driven inflow of warm deep water. *Nat. Commun.* **7:12300**, (2016).
- 150 7. Palóczy, A., Gille, S. T. & Mcclean, J. L. Oceanic Heat Delivery to the Antarctic
151 Continental Shelf : Large-Scale , Low-Frequency Variability. *J. Geophys. Res.* **123**,
152 7678–7701 (2018).
- 153 8. Assmann, K. M., Darelius, E., Wåhlin, A. K., Kim, T. W. & Lee, S. H. Warm
154 Circumpolar Deep Water at the western Getz Ice Shelf Front, Antarctica. *Geophys.*
155 *Res. Lett.* **46**, 870–878 (2019).
- 156 9. Jenkins, A. *et al.* West Antarctic Ice Sheet retreat in the Amundsen Sea driven by
157 decadal oceanic variability. *Nat. Geosci.* (2018). doi:10.1038/s41561-018-0207-4
- 158 10. IPCC. *Climate Change 2014: Synthesis Report. Contribution of Working Groups I, II*
159 *and III to the Fifth Assessment Report of the Intergovernmental Panel on Climate*
160 *Change.* (IPCC, 2014).
- 161 11. IMBIteam. Mass balance of the Antarctic ice sheet from 1992 to 2017. *Nature* **558**,
162 219–222 (2018).
- 163 12. DeConto, R. M. & Pollard, D. Contribution of Antarctica to past and future sea-level
164 rise. *Nature* **531**, 591–597 (2016).
- 165 13. Scambos, T. A., Bohlander, J. A., Shuman, C. A. & Skvarca, P. Glacier acceleration
166 and thinning after ice shelf collapse in the Larsen B embayment, Antarctica. *Geophys.*
167 *Res. Lett.* **31**, 2001–2004 (2004).
- 168 14. Jenkins, A. *et al.* Observations beneath Pine Island Glacier in West-Antarctica and
169 implications for its retreat. *Nat. Geosci.* **3**, 468–472 (2010).
- 170 15. Callahan, J. E. The structure and circulation of Deep Water in the Antarctic. *Deep Sea*

- 171 *Res.* **19**, 563–575 (1972).
- 172 16. Thompson, A. F., Stewart, A. L., Spence, P. & Heywood, K. J. The Antarctic Slope
173 Current in a Changing Climate. *Rev. Geophys.* **56**, 741–770 (2018).
- 174 17. Depoorter, M. A. *et al.* Calving fluxes and basal melt rates of Antarctic ice shelves.
175 *Nature* **502**, 89–92 (2013).
- 176 18. Wåhlin, A. K., Yuan, X., Björk, G. & Nohr, C. Inflow of Warm Circumpolar Deep
177 Water in the Central Amundsen Shelf*. *J. Phys. Oceanogr.* **40**, 1427–1434 (2010).
- 178 19. Herraiz-Borreguero, L. *et al.* Circulation of modified Circumpolar Deep Water and
179 basal melt beneath the Amery Ice Shelf, East Antarctica. *J. Geophys. Res. Ocean.* **120**,
180 3098–3112 (2015).
- 181 20. Nakayama, Y., Menemenlis, D., Zhang, H., Schodlok, M. & Rignot, E. Origin of
182 Circumpolar Deep Water intruding onto the Amundsen and Bellingshausen Sea
183 continental shelves. *Nat. Commun.* **9**, 1–9 (2014).
- 184 21. St-Laurent, P., Klinck, J. M., Dinniman, M. S. & Oceanography, C. P. On the Role of
185 Coastal Troughs in the Circulation of Warm Circumpolar Deep Water on Antarctic
186 Shelves. *J. Phys. Oceanogr.* **43**, 51–64 (2013).
- 187 22. Cushman-Roisin, B. & Beckers, J.-M. *Introduction to Geophysical Fluid Dynamics: Physical and numerical aspects.* (Prentics-Hall Inc., 2011).
- 188
- 189 23. Nof, D. The translation of isolated cold eddies on a sloping bottom. *Deep. Res. Part A-
190 Oceanographic Res. Pap.* **30**, 171–182 (1983).
- 191 24. Wåhlin, A. K. Topographic advection of dense bottom water. *J. Fluid Mech.* **510**, 95–
192 104 (2004).
- 193 25. Ha, H. K. *et al.* Circulation and Modification of Warm Deep Water on the Central
194 Amundsen Shelf. *J. Phys. Oceanogr.* **44**, 1493–1501 (2014).
- 195 26. Wåhlin, A. K. *et al.* Variability of Warm Deep Water Inflow in a Submarine Trough on
196 the Amundsen Sea Shelf. *J. Phys. Oceanogr.* **43**, 2054–2070 (2013).
- 197 27. Kalén, O. *et al.* Is the oceanic heat flux on the central Amundsen sea shelf caused by
198 barotropic or baroclinic currents? *Deep. Res. Part II Top. Stud. Oceanogr.* (2016).
199 doi:10.1016/j.dsr2.2015.07.014

- 200 28. Rignot, E., Jacobs, S., Mouginot, J. & Scheuchl, B. Ice-Shelf Melting Around
201 Antarctica. *Science (80-.)*. **341**, 266–270 (2013).
- 202 29. Grosfeld, K., Gerdes, R. & Determann, J. Thermohaline circulation and interaction
203 between ice shelf cavities and the adjacent open ocean. *J. Geophys. Res. Ocean.* **102**,
204 15595–15610 (1997).
- 205 30. Jacobs, S. *et al.* Getz Ice Shelf Melting Response to Changes in Ocean Forcing. *J.*
206 *Geophys. Res. - Ocean.* **118**, 4152–4168 (2013).
- 207 31. Arndt, J. E. *et al.* The International Bathymetric Chart of the Southern Ocean (IBCSO)
208 Version 1.0 - A new bathymetric compilation covering circum-Antarctic waters.
209 *Geophys. Res. Lett.* **40**, 311–3117 (2013).
- 210 32. Little, C. M., Gnanadesikan, A. & Oppenheimer, M. How ice shelf morphology
211 controls basal melting. *J. Geophys. Res.* **114**, C12007 (2009).
- 212 33. Miles, T. *et al.* Glider observations of the Dotson Ice Shelf outflow. *Deep Sea Res.*
213 *Part II Top. Stud. Oceanogr.* **123**, 16–29 (2015).
- 214 34. Nicholls, K. W. *et al.* Measurements beneath an Antarctic ice shelf using an
215 autonomous underwater vehicle. **33**, 2–5 (2006).
- 216 35. Gade, H. Melting of ice in sea water: A primitive model with application to the
217 Antarctic ice shelf and icebergs. *J. Phys. Oceanogr.* **9**, 189–198 (1979).

218

219 **Acknowledgments:**

220 The experiments were supported by the European Community's H2020 through the grant to
221 HYDRALAB-PLUS, Contract no. 654110. We gratefully acknowledge grant support for the
222 authors as follows: ED and NS, Norwegian Research Council through grant no. 267660
223 (TOBACO) and 231549 (WARM); AJ from the UK Natural Environment Research Council
224 through grant no. NE/L013770/1 (FISS), AW from the Swedish Research Council and the
225 Swedish Foundation for Strategic Research through the Swedish Maritime Robotics Center
226 (SMaRC), TWK from the Korea Polar Research Institute grant KOPRI PE19060. Thanks to I.
227 Fer for lending instrumentation to GW1 and GW2.

228

229

230 **Author contributions:**

231 AKW proposed the research. AKW, NS, ED and KA wrote the first draft. JS assisted with
232 analyses and repository of laboratory data. All authors contributed to the laboratory
233 experiments, to data processing, and/or to the field work. AKW, NS, SV, AKM prepared the
234 figures. All authors read and commented on the text.

235

236 **Author information:**

237 Corresponding author: Dr. A.K. Wåhlin, email: awahlin@gu.se

238 No authors have any competing interests.

239

240 **Author affiliations:**

241 Wåhlin, A. K.: Department of Marine Sciences, University of Gothenburg, Sweden

242 Steiger, N.: Bjerknes Centre for Climate Research and Geophysical Institute, University of
243 Bergen, Norway

244 Darelius, E.: Geophysical Institute, University of Bergen, Norway

245 Assmann, K.M.: Department of Marine Sciences, University of Gothenburg, Sweden

246 Glessmer, M.S.: Leibniz Institute of Science and Mathematics Education, Kiel, Germany

247 Ha, H.K., Inha University, South Korea

248 Herraiz-Borreguero, L., Commonwealth Scientific and Industrial Research Organisation
249 (CSIRO), Hobart, Australia

250 Heuzé, C.: Department of Earth Sciences, University of Gothenburg, Sweden

251 Jenkins, A., British Antarctic Survey, Cambridge, United Kingdom

252 Kim, T.W., Korea Polar Research Institute, South Korea

253 Mazur, A.K.: Department of Marine Sciences, University of Gothenburg, Sweden

254 Sommeria, J., Laboratoire des Ecoulements Geophysiques et Industriels

255 Domaine Universitaire, Grenoble, France

256 Viboud, S.: Laboratoire des Ecoulements Geophysiques et Industriels

257 Domaine Universitaire, Grenoble, France

258

259 **Table 1. Correlation between Getz moorings**

260

	ρ_B GW1	T_B GW2	ρ_B GW3	U GW3
T_B GW2	0.62 (0.55)	-	-	-
ρ_B GW3	0.67 (0.58)	0.92 (0.83)	-	-
U_{BC} GW1	0.54 (0.46)	0.71 (0.62)	0.77 (0.67)	0.66 (0.53)
U_{BT} GW1	-0.09 (-0.03)	-0.08 (0.05)	-0.25 (-0.1)	-0.08 (0.02)
U_{BC} GW2	0.43 (0.36)	0.54 (0.49)	0.53 (0.45)	0.67 (0.51)
U_{BT} GW2	0.15 (0.03)	0.20 (0.01)	0.09 (0.1)	0.23 (0.23)
U GW3	0.51 (0.36)	0.5 (0.39)	0.65 (0.57)	-

261

262 Correlation coefficients between combinations of bottom density ρ_B (or bottom temperature
 263 T_B for GW2, which had a broken conductivity sensor and hence no bottom density) and along-
 264 slope bottom velocity U , as well as the barotropic (U_{BT}) and baroclinic (U_{BC}) components of
 265 bottom velocity for the three moorings GW1, GW2 and GW3. Numbers shown are
 266 correlations between the indicated quantities based on 10-day average values and, within
 267 parentheses, 3-day averages. Bold numbers indicate that the correlations are significant at the
 268 99.99% level. Dark blue fields indicate the key correlations discussed in the text.

269

270 **Captions:**

271 **Figure 1. Blocking of topographically steered current at the Getz Ice Shelf front.** (a)

272 Mooring locations and time averaged velocities from three moorings (GW1-3) are shown as
273 feather plots on top of the local bathymetry³¹. Velocities are color coded with conservative
274 temperature θ and depth-averaged in 50 m bins starting at the bottom. The lowermost (red,
275 warmest) and uppermost (blue, coldest) bin depths are quoted near the corresponding arrow.
276 Also shown is the location of the ice front in January 2016, 2017 and 2018 (blue lines,
277 Methods). Lower panels show conservative temperature θ versus absolute salinity S_A for (b)
278 GW1 (c) GW2 (d) GW3 in green hues, gray dots are the data from all moorings. Red squares
279 indicate Circumpolar Deep Water temperature- and salinity range¹⁵, blue thick line is the
280 mixing line between CDW and glacier meltwater³⁵, lower black thin line is the freezing point
281 (T_f). The lack of data points near salinity 34.5 g kg^{-1} in GW2 is due to the fact that GW2 only
282 had two salinity sensors (Extended Data Figure 2), of which one was faulty for a period of
283 time (see Methods). Mooring temperature- and velocity time series are shown in Extended
284 Data Figs. 1 - 3.

285

286 **Figure 2: Baroclinic velocity component at GW2 is similar to total velocity at GW3.**

287 Three-day average along-slope velocity (color bar, m/s), with isotherms (black contours,
288 every 0.5 degrees, thick black line shows the 0 degree isotherm) (a) Total alongslope velocity
289 at GW2 (b) Baroclinic velocity component (Methods) at GW2 (c) Total alongslope velocity at
290 GW3. Note that the topmost sensor on GW2 was at 357 m depth while at GW3 it was at 288
291 m depth (Extended Data Figure 2, Extended Data Figure 3).

292

293 **Figure 3. Experimental set-up and difference between barotropic and baroclinic flow.**

294 (a) Sketch of the experiment. Side view sketches of the ice shelf (light gray), bottom (dark
295 gray) and water (blue) with ice shelf draft 0 cm (b) 30 cm (c) and tilted (d). Photographs are
296 from from underneath the ice shelf, facing out, for (e) barotropic flow and (f) baroclinic flow.

297

298 **Figure 4: Blocking of depth-independent currents in laboratory.** Horizontal velocities

299 from the laboratory experiments are presented for the barotropic flow with the three different
300 ice shelf configurations (Fig. 3b-d). Colors indicate velocity in the y-direction, arrows indicate
301 velocity vectors. (a)-(c) show velocities at the horizontal plane in the center of the current
302 (black lines in (d)-(i)), (d)-(f) show velocities at vertical sections underneath the ice shelf

303 (green lines in (a)-(c)) and (g)-(i) in front of it (magenta lines in (a)-(c)). Dashed and
304 shadowed rectangles indicate the ice shelf, grey shading indicates topography and grey lines
305 are lines of constant water thickness that the current is expected to follow. White areas are not
306 measured/ missing data. The cyan arrow beneath the scale arrow in (a) - (c) indicate the
307 temporal standard deviation of the velocity and magenta bar indicates the error (Methods).

308 **Methods**

309 **Mooring data**

310 Three moorings were deployed on 29 January 2016 and recovered on 18 January 2018 on the
311 western flank of Siple Island (Fig. 1). Two of the moorings were deployed 11-14 km from the
312 ice shelf at depths of 600 m (GW2, 73°47.6' S, 127°36.0'S) and 700 m (GW1, 73° 49.8' S,
313 127° 47.6'S). The third mooring was located 700-750 m from the ice shelf at a depth of 600 m
314 (GW3, 73° 50.0' S, 127°16.6'S), within a Rossby radius (2 km) of the ice front. The moorings
315 were equipped with sensors for temperature, conductivity and pressure from Seabird
316 Electronics (SBE37, SBE39 and SBE56) and Acoustic Doppler Current Profilers (ADCP,
317 Teledyne RD Instruments, 75 and 150 kHz kHz Sentinel). The initial accuracy of the
318 temperature data were 0.002 °C and the resolution was 0.0001 °C. The ADCP data were
319 quality controlled using standard criteria for filtering out bad data and outliers³⁶ based on
320 quality controls on individual beams and bins recorded by the instrument each ping (percent
321 good returns below 50%, average echo intensity below 40 (counts) and roll and pitch of
322 instrument exceeding 20° filtered out). The raw data (saved at 15 minute temporal resolution)
323 had standard error 1 -1.5 cm/s and were averaged to hourly means.

324 Hydrographic measurements extended from the bottom to 357 and 305 m below the surface
325 for GW2 and GW1, respectively, with downward looking ADCPs just above the top sensor,
326 and to 288 m below the surface at GW3, with an upward looking ADCP just below the
327 bottom sensor (Fig. 1). Extended Data Figures 1 - 3 show the North- and Eastward velocities
328 recorded at the three locations, together with temperature. Conservative temperature and
329 absolute salinity in Fig. 1 were calculated following TEOS-10³⁷

330 The along-slope directions were defined as true bearings of 135° for GW1, 110° for GW2,
331 and 70° for GW3, based on the IBCSO³¹ database (Fig. 1).

332

333 **Ice shelf data**

334 The position of the ice front shown in Figure 1 was manually digitized from Sentinel-1
335 Synthetic Aperture Radar images recorded in January of 2016, 2017 and 2018. Level-1
336 Ground Range Detected images, projected to ground range using the Earth ellipsoid model
337 WGS84 with pixel size of 40x40 m. Getz ice shelf is characterized by surface structures
338 parallel to the calving front³⁸. This is the most common pattern observed among west
339 Antarctic ice shelves and gives the type of calving front studied. The mean ice equivalent
340 thickness of Getz ice shelf is 286 m³, comparable to the average of ice shelves in the
341 Amundsen Sea (273 m). This indicates that Getz ice shelf is representative for the area.

342 **Baroclinic and barotropic velocity components**

343 According to thermal wind balance²² the baroclinic velocity component is expected to be
344 largest in the dense layer below the thermocline and small in the well-mixed water above it.
345 Since the present velocity data do not cover the upper water column (Extended Data Fig. 1)
346 the barotropic (U_{BT}) and baroclinic (U_{BC}) velocity components have to be estimated based on
347 the data at hand. Three different methods were employed and compared,

348 (i) Assuming that the barotropic velocity component is given by the vertical average of the
349 measured water column. While this method would give an accurate estimate in flows that
350 have a comparatively thin baroclinic layer and/or a strong barotropic current, it will likely
351 overestimate the barotropic current in the present data since only the bottom half of the water
352 column is measured.

353 (ii) Assuming that the barotropic velocity component is given by the vertical average of the
354 velocity from 150 m above the seabed to the upper end of the measured volume. This method
355 will give an accurate estimate when the thermocline is closer than 150 m to the seabed but
356 will otherwise overestimate the barotropic velocity component.

357 (iii) Assuming that the barotropic velocity component is given by the average velocity in the
358 water above the thermocline. This method gives the most accurate result, but a disadvantage
359 is that the thermocline was not always covered by the mooring data. By choosing the
360 thermocline level to be at -0.5 °C, barotropic velocity estimates were obtained for nearly the
361 complete record (Extended Data Fig. 1, lower panels).

362 Using any of the above methods, U_{BT} and U_{BC} can be calculated by

$$U_{BC}(z,t) = U(z,t) - U_{BT}(t)$$
$$U_{BT}(t) = \frac{1}{(Z_0 - Z_1)} \int_{Z_0}^{Z_1} U(\xi,t) d\xi \quad (1)$$

364 where $U(z,t)$ is the velocity measured at the moorings for various depths z and times t , ξ is the
365 integration variable, and the integral limits Z_0 and Z_1 are given by one of the following²⁷:

- 366 (i) Z_0 = seabed and Z_1 is the upper end of the measured water column.
367 (ii) Z_0 = 150 m above the seabed and Z_1 is the upper end of the measured water column
368 (iii) Z_0 is the -0.5 °C isotherm and Z_1 is the upper end of the measured water column

369 Extended Data Figure 4 shows time series of the three estimates (i) - (iii) of the barotropic
370 velocities over the two years. Extended Data Figure 5 shows the average velocity (thick lines)
371 together with the three alternative barotropic components (thin lines Extended Data Fig. 5A),
372 the baroclinic component (Extended Data Fig. 5B) and the temperature (Extended Data Fig.

373 5C). In Figure 2 the barotropic velocity component was defined according to (ii) above, i.e.
 374 red lines in Extended Data Figure 4 and dashed lines in Extended Data Figure 5A. Similar
 375 results were obtained using the other two definitions of Z_0 and Z_1 , which is in accordance with
 376 [27].

377

378 **Heat transport calculations**

379 Assuming that the width of the flow is bounded by the sloping topography (as suggested by
 380 the laboratory experiments), the heat transport H [J/s] toward the glacier can be estimated by

$$381 \quad H = W \int_D^\eta \rho C_P U (T - T_{REF}) d\xi, \quad (2)$$

382 where W [m] is the width of the sloping channel side, D is the bottom elevation, η is the top
 383 of the mooring, ρ [kg m^{-3}] is density, C_P [$\text{J K}^{-1} \text{kg}^{-1}$] is the specific heat capacity, U [m s^{-1}] is
 384 the (average) along-channel velocity, T [K] the temperature and T_{REF} the temperature to which
 385 the water cools after interaction with glacial ice. Assuming that all the water cools to freezing
 386 temperature, (2) is given by

$$387 \quad H = W \rho C_P \int_D^\eta U (T - T_F) dz.$$

388 where T_F [K] is the in situ freezing temperature (which decreases with pressure and salinity).
 389 The heat flux induced by the barotropic respectively baroclinic velocity components is then
 390 given by $H = H_{BT} + H_{BC}$ where

$$391 \quad H_{BC} = W \rho C_P \int_D^\eta U_{BC} (T - T_F) dz \quad (3)$$

$$392 \quad H_{BT} = W \rho C_P \int_D^\eta U_{BT} (T - T_F) dz, \quad (4)$$

393 and the barotropic (U_{BT}) and baroclinic (U_{BC}) velocity components are given by (1). In
 394 Extended Data Figure 6, time series of H , H_{BT} and H_{BC} were calculated using $W = 10$ km, C_P
 395 = $3.968 \text{ kJ kg}^{-1} \text{ K}^{-1}$, *in situ* freezing temperature³⁹, *in situ* density³⁹, and definition (ii) for the
 396 barotropic velocity (1). The temperature- and velocity data were re-gridded to a common grid
 397 using daily averages and linear interpolation in the vertical with 8 m cell size.

398 Extended Data Table 1 shows the temporal average of the heat flux calculated from (2) - (4)
 399 and each of the three methods (i) - (iii). As discussed, the barotropic velocity is likely
 400 overestimated with method (i) which gives smaller baroclinic heat flux components for all

401 three moorings. The results of method (ii) and (iii) are quite consistent and shows that the
 402 baroclinic heat flux is about 30% at GW1 and GW2 while it is between 90% - 97% at GW3,
 403 where the average barotropic velocity is nearly zero.

404

405 **Heat transport errors**

406 The instrument error in the ADCP is maximum 1.5 cm/s and the real error is significantly
 407 lower since an average over many pings was used. This error is of the same order of
 408 magnitude as the methodological uncertainty, exemplified by the three methods (Extended
 409 Data Fig. 5). In the conversion from velocity to heat transport there is an error involved in the
 410 assumption that the data at the mooring site is representative for the entire channel (equation
 411 (2)). In the absence of continuous, high resolution sampling across the width of the channel,
 412 which would enable an exact estimate of this error, an indication of the uncertainties involved
 413 can be obtained by the difference between the results of GW1 and GW2 (Table 1), i.e. about
 414 0.5 TW or 18%. There is also an error caused by the fact that the upper part of the water
 415 column is not included in the heat flux calculations. Since the temperature above the
 416 measured volume is near freezing temperature (Extended Data Fig. 5), however, this error is
 417 relatively small.

418 Another source of error is the assumption that the flow is steady. By separating velocity and
 419 temperature into mean and fluctuating components the impact of temporal variability on the
 420 average heat transport can be estimated by

$$421 \quad \overline{H} = W\rho C_p \int_D^{\eta} \overline{(\overline{U} + U')(T + T' - T_F)} d\xi, \quad (5)$$

422 where temporal mean is denoted by overbar and fluctuating part is denoted by hyphen. Since
 423 the temporal average of the fluctuating part is zero, (5) reduces to

$$424 \quad \overline{H} = W\rho C_p \int_D^{\eta} (\overline{\overline{U}(T - T_F)} + \overline{U'T'}) d\xi = \overline{\overline{H}} + \tilde{H}, \quad (6)$$

425 where $\overline{\overline{H}}$ is the contribution from the average velocity and temperature, and \tilde{H} is the
 426 contribution from the temporal variability about the mean. Extended Data Table 1 shows the
 427 two contributions - the heat flux in all three moorings is caused primarily by the mean and the
 428 contribution from the fluctuations is between 6% and 20%.

429

430 **Theory**

431 In geostrophic flow²⁰ the momentum equations are dominated by the Coriolis- and the
 432 pressure gradient terms, i.e.

$$433 \quad v = \frac{1}{f\rho} \frac{\partial p}{\partial x} \quad (7)$$

$$434 \quad u = -\frac{1}{f\rho} \frac{\partial p}{\partial y}, \quad (8)$$

435 where (u, v) are the velocity components in the (x, y) directions, f (s^{-1}) is the Coriolis
 436 parameter and p is the hydrostatic pressure. Assuming that the Coriolis parameter is constant
 437 and using the Boussinesq approximation²², it follows from (7) - (8) that geostrophic velocity
 438 is non-divergent, i.e.

$$439 \quad \frac{\partial u}{\partial x} + \frac{\partial v}{\partial y} = 0. \quad (9)$$

440 For the simplified case of one active layer, i.e. a well-mixed layer extending from the bottom
 441 to either the surface or to the interface separating an active dense layer from an inactive
 442 lighter water mass above it, vertical integration of the continuity equation gives²⁰⁻²² (using (9)
 443 and the fact that the velocities are vertically homogeneous)

$$444 \quad \frac{\partial \eta}{\partial t} + u \frac{\partial \eta}{\partial x} + v \frac{\partial \eta}{\partial y} - u \frac{\partial D}{\partial x} - v \frac{\partial D}{\partial y} = 0, \quad (10)$$

445 where η is the upper surface (either the water surface or the dense interface) and D is the
 446 bottom elevation. Equation (10) can also be expressed in terms of the layer thickness
 447 $H(x, y, t) = \eta(x, y, t) - D(x, y)$ according to

$$448 \quad \frac{\partial H}{\partial t} + u \frac{\partial H}{\partial x} + v \frac{\partial H}{\partial y} = 0. \quad (11)$$

449 Steady solutions to (11) have streamlines parallel to lines of constant water column thickness
 450 (H), irrespective of the bottom elevation $D(x, y)$ and the pressure (as long as the flow is
 451 geostrophic). Equation (11) might appear trivial but the combination of geostrophy and solid
 452 upper and lower boundaries has important consequences for the currents entering ice shelf
 453 cavities in Antarctica. When an ice shelf is protruding from above, the along-trough flow
 454 experienced outside the cavity will be deflected to flow along the ice front instead. Barotropic
 455 flow towards Antarctica's ice shelves is thus expected to be blocked from reaching the inner
 456 parts of the ice shelf cavities (as seen in Fig. 1). Baroclinic flow, on the other hand, is
 457 expected to follow the depth contours into the inner ice shelf cavity.

458

459 **Laboratory experiments**

460 The laboratory experiments were conducted on the 13-m-diameter rotating platform at
461 Laboratoire des Écoulements Géophysiques et Industriels (LEGI) in Grenoble, France.

462 A v-shaped channel of size 5 m × 1 m × 0.5 m and a 2% slope (Extended Data Fig. 7) was
463 built at the center of the turntable (red dot Extended Data Fig. 7). Focusing on the dynamics
464 of the flow and ignoring thermodynamic changes such as melting and freezing of ice, a
465 cuboid Plexiglas ice shelf with adjustable elevation and tilt was placed at the lower (closed)
466 end of the channel. The tank was filled with 90 cm of fresh water and rotated clockwise
467 (Southern Hemisphere) with a rotation period of 30 s, giving a Coriolis parameter $f = 0.42 \text{ s}^{-1}$.

468 A source, placed in the center of the left-hand flank of the channel (looking towards the ice
469 shelf) and resting on the topography, pumped water at 60 l/min into the channel. The source
470 was 0.15 m high, 0.25 m wide, 0.25 m long and sloped at the bottom to fit the topography
471 (Extended Data Fig. 7). The outflow area was 0.47 m² and had a honeycomb of small tubes to
472 produce a homogeneous laminar flow. For the barotropic experiments the source water was
473 fresh like the ambient water and for the baroclinic experiments it was saline and 2 kg m⁻³
474 denser than the ambient water. A drainage and skimmer kept the water level constant.

475 Neutrally buoyant particles (60 μm Dantec Dynamics particles) in the source water were
476 illuminated by a horizontal laser plane (Extended Data Fig. 8) in order to visualize the flow.

477 Two cameras with pixel resolution 2560 × 2160 pixels were mounted above the channel. The
478 footprint of both cameras (Extended Data Fig. 7) gave a resolution of 0.6 mm/pixel. The laser
479 shifted through depth levels starting near the bottom of the channel. For the barotropic
480 experiments 12 different depth levels were used with a vertical distance of $dz = 6.2 \text{ cm}$. In
481 order to resolve better the faster-moving dense current and focus on the lower part of the
482 channel, 7 different depth levels with $dz = 5.8 \text{ cm}$ were used in the baroclinic experiments. At
483 each level, 30 (barotropic experiments) or 20 (baroclinic experiments) consecutive images
484 were taken by both cameras with 0.1 s interval giving a total of 60 s for a complete cycle
485 through all depth levels. The obtained images were used for Particle Image Velocimetry (PIV)
486 calculations with the UVMAT software developed at LEGI (for details see
487 <http://servforge.legi.grenoble-inp.fr/projects/soft-uvmat>). Independent results were also
488 obtained with a second software, MatPIV
489 (<https://www.mn.uio.no/math/english/people/aca/jks/matpiv>), and found to agree with
490 UVMAT. Using the pixel per image value, i.e. 0.6 mm/0.5 s for barotropic (every 5 images
491 were used) and 0.6 mm/0.1 s for baroclinic experiments, the velocity error was 1.2 mm/ for
492 the barotropic and 6 mm/s for the baroclinic experiments. The obtained 25 (or 19 for
493 baroclinic experiments) velocity fields for each level were then averaged, which lowered the

494 error further. Figure 4 shows the average of 4-5 cycles at one level, starting at the time when
495 the leading edge reached the ice front, together with the temporal standard deviation of the
496 velocity for that level (cyan arrows) and the error (magenta bars). Outliers (defined as
497 velocities for which the standard deviation exceeds 10 times the average standard deviation)
498 were identified and filtered out. The vertical sections (Fig. 4d-f) were created from the parts
499 of the horizontal slices that occupied +/- 2 cm around the green and magenta lines in Fig. 4.

500 In addition to the top-view cameras, a side-view camera was mounted outside a glass wall at
501 the side of the tank and GoPro cameras were lowered into the water to get side-view images
502 (Fig. 3 and Extended Data Fig. 8). In the side view images, fluorescent dye (rhodamin) was
503 used for visualization.

504 The topography was built to mimic a submarine trough topography with depth variations of
505 same magnitude as the ice shelf draft, in similarity with the observations. Geostrophic balance
506 was ensured by choosing flow- and rotation rates so that both the Ekman number Ek (i.e. the
507 frictional force compared to the Coriolis force²⁰) and the Rossby number²⁰ (i.e. the inertial
508 forces compared to the Coriolis force) were smaller than one. The values of the various scales
509 and the non-dimensional numbers are shown in Extended Data Table 1. While the Ekman
510 number was clearly negligible (0.002-0.004), the Rossby number was 0.14-0.2 meaning that
511 ageostrophic effects may amend the process, particularly in regions where the velocity might
512 be larger.

513 Before each experiment the platform was spun up for 2-3 hours to reach solid body rotation,
514 which was determined by observing the movement of particles. Each experiment was started
515 by opening the source. After about 5 - 10 minutes (faster for baroclinic flow) a current
516 moving towards the ice shelf developed over the sloping part of the topography (Extended
517 Data Fig. 8). Behind the leading edge of the current a semi-steady flow with regions of slower
518 and faster flow moving in the direction of the ice shelf developed (Extended Data Fig. 8d).
519 After interaction with the ice-shelf (15-30 min after experiment start) a counter-current on the
520 opposite side developed, after which the experiment ended.

521 The baroclinic flow developed faster, was more steady, and was not influenced by the
522 presence of the ice shelf. Instead of returning on the opposite side, the baroclinic flow slowly
523 filled the ice shelf cavity with dense water (Extended Data Fig. 8). More details from the
524 experiments, including detailed drawings, diary, etc is provided at
525 <http://servforge.legi.grenoble-inp.fr/projects/pj-coriolis-17iceshelf>

526

527 **Methods references**

- 528 36. Taylor, J. A. & Jonas, A. M. Maximising Data Return: Towards a quality control
529 strategy for Managing and Processing TRDI ADCP Data Sets from Moored
530 Instrumentation. in *2008 IEEE/OES 9th Working Conference on Current Measurement*
531 *Technology* 80–88 (IEEE, 2008). doi:10.1109/CCM.2008.4480848
- 532 37. IOC, SCOR & IAPSO. *The International thermodynamic equation of seawater, 2010:*
533 *calculation and use of thermodynamic properties. IOC: Manuals and guides (UNESCO*
534 *Digital Library)* (2010).
- 535 38. Wesche, C., Jansen, D. & Dierking, W. Calving Fronts of Antarctica: Mapping and
536 Classification. *Remote Sens.* **5**, 6305–6322 (2013).
- 537 39. Fofonoff, N. P. & Millard, R. C. *Algorithms for Computation of Fundamental*
538 *Properties of Seawater. UNESCO Technical Papers in Marine Science* (1983).
- 539 40. Darelius, E., Fer. I., Assmann, K. M. & Kim, T. W. Physical oceanography from
540 Mooring UiB1 and UiB4 in the Amundsen Sea. (2018). doi:10.21335/NMDC-
541 1721053841

542

543 **Data and code availability:**

544 The mooring data analysed during the current study (raw data for Figure 1-2 and extended
545 data Figures 1-6) are available at the Norwegian Marine Data Centre
546 (<https://doi.org/10.21335/NMDC-1721053841>⁴⁰, GW1-2) and at SOOS data base at NODC
547 (<https://doi.org/10.25921/n07g-f935> and <https://doi.org/10.25921/6pwp-1791>, GW3)

548 Raw data obtained from the PIV calculations (raw data for Figure 4 and Extended Data Figure
549 9) are available at Zenodo (<https://zenodo.org/record/3543624>).

550 The PIV calculations were conducted with the matlab software UVMAT developed at LEGI
551 available at <http://servforge.legi.grenoble-inp.fr/projects/soft-uvmat>. Independent results were
552 also obtained with the MatPIV package available at
553 <https://www.mn.uio.no/math/english/people/aca/jks/matpiv>.

554

555

556 **Extended data legends**

557 **Extended Data Figure 1: Two year time series of velocity and temperature from GW1**
558 **mooring.** Time series of (a) eastward velocity, (b) northward velocity and (c) temperature for
559 the GW1 mooring. Black lines in (c) indicate positions of Microcats (thick lines) and SBE56
560 (thin lines).

561 **Extended Data Figure 2: Two year time series of velocity and temperature from GW2**
562 **mooring.** Time series of (a) eastward velocity, (b) northward velocity and (c) temperature for
563 the GW2 mooring. Black lines in (c) indicate positions of Microcats (thick lines) and SBE56
564 (thin lines).

565 **Extended Data Figure 3: Two year time series of velocity and temperature from GW3**
566 **mooring.** Time series of (a) eastward velocity, (b) northward velocity and (c) temperature for
567 the GW3 mooring. Black lines in (c) indicate positions of Microcats (thick lines) and SBE56
568 (thin lines).

569 **Extended Data Figure 4: Comparison of methods for calculating barotropic component.**
570 Along-slope barotropic current component based on option (i): vertical average, option (ii):
571 vertical average of the water more than 150 m above seabed, and option (iii): vertical average
572 of water above the -0.5° isotherm according to legend. (a) Mooring GW1, 3-day averaged (b)
573 Mooring GW2, 3-day averaged (c) Mooring GW3, 3-day averaged.

574 **Extended Data Figure 5: The barotropic velocity is larger for GW1 and GW2 than**
575 **GW3, the baroclinic velocity and the temperature increase towards the bottom.** (a) Thick
576 lines show average along-slope velocities as a function of distance above bottom, with colors
577 indicating mooring (legend). Thin vertical lines show the barotropic components estimated
578 according to method (i) (dotted lines), method (ii) (dashed lines), and method (iii) (solid
579 lines). (b) Baroclinic velocity components as a function of distance above bottom. (c) Average
580 temperature as a function of distance above bottom.

581 **Extended Data Figure 6: The barotropic heat flux component is larger than the**
582 **baroclinic for GW1 and GW2.** Time series of total heat flux and the barotropic and
583 baroclinic components using expression (2) and definition (ii) of barotropic velocity. (a)
584 Mooring GW1 (b) Mooring GW2 (c) Mooring GW3.

585 **Extended Data Figure 7. Experiment set-up and dimensions.** (a) Top view drawing of v-
586 shaped channel (blue), ice shelf (white), camera views (PCO1, green, PCO2, orange) and the
587 source (to scale). (b) Side view drawing looking into the ice shelf facing South (c) Side view
588 drawing looking East (d)-(f) Top views of topography (gray scale, color bar) and water

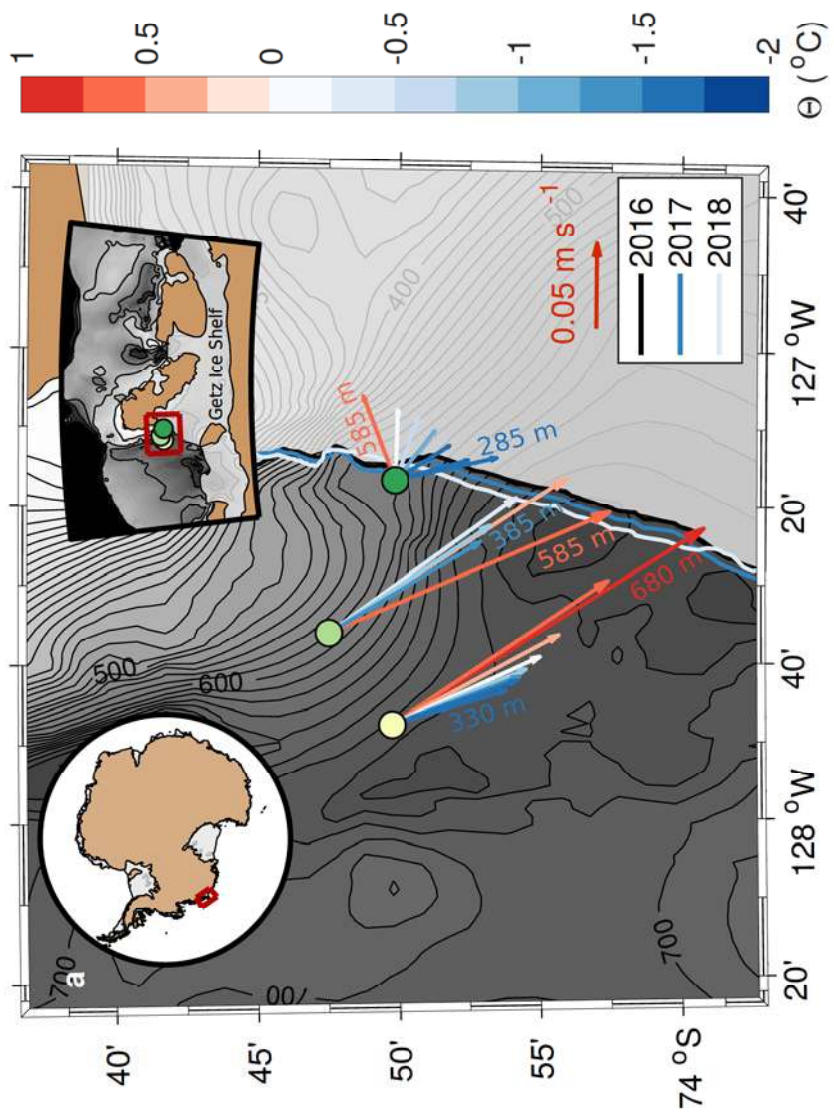
589 column thickness (colored lines, labels) for (d) Ice shelf draft 0 cm (e) Ice shelf draft 30 cm,
590 tilted (f) ice shelf draft 30 cm, horizontal.

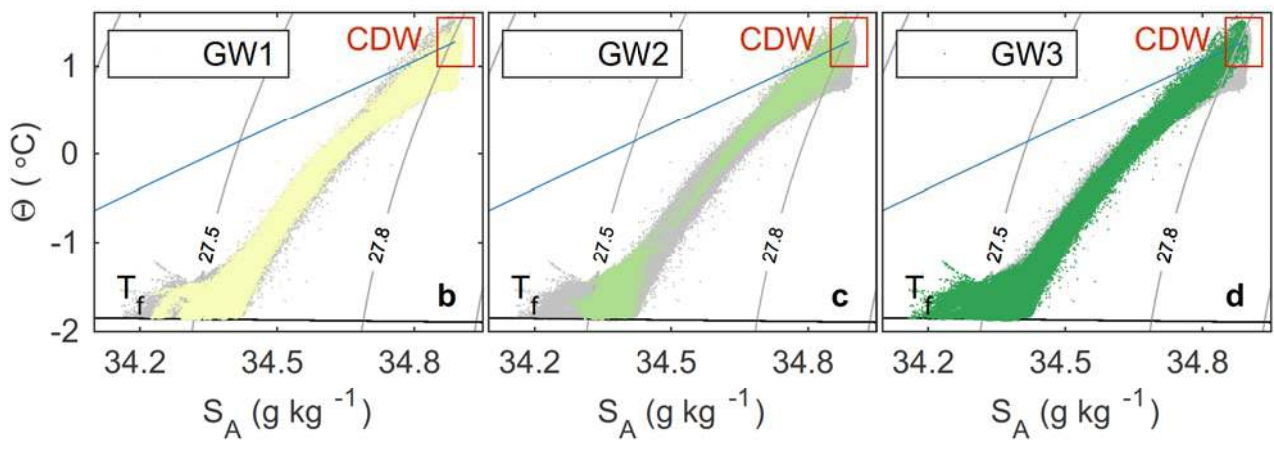
591 **Extended Data Figure 8: Photographs from the experiments.** (a) Top view showing the
592 experimental set-up with the horizontal and vertical laser sheets. (b) Technicians and students
593 preparing for an experiment (c) Time series showing the ice shelf cavity filling up with dense
594 water for the baroclinic experiments (d) Top view photograph showing a barotropic current
595 moving towards the ice shelf.

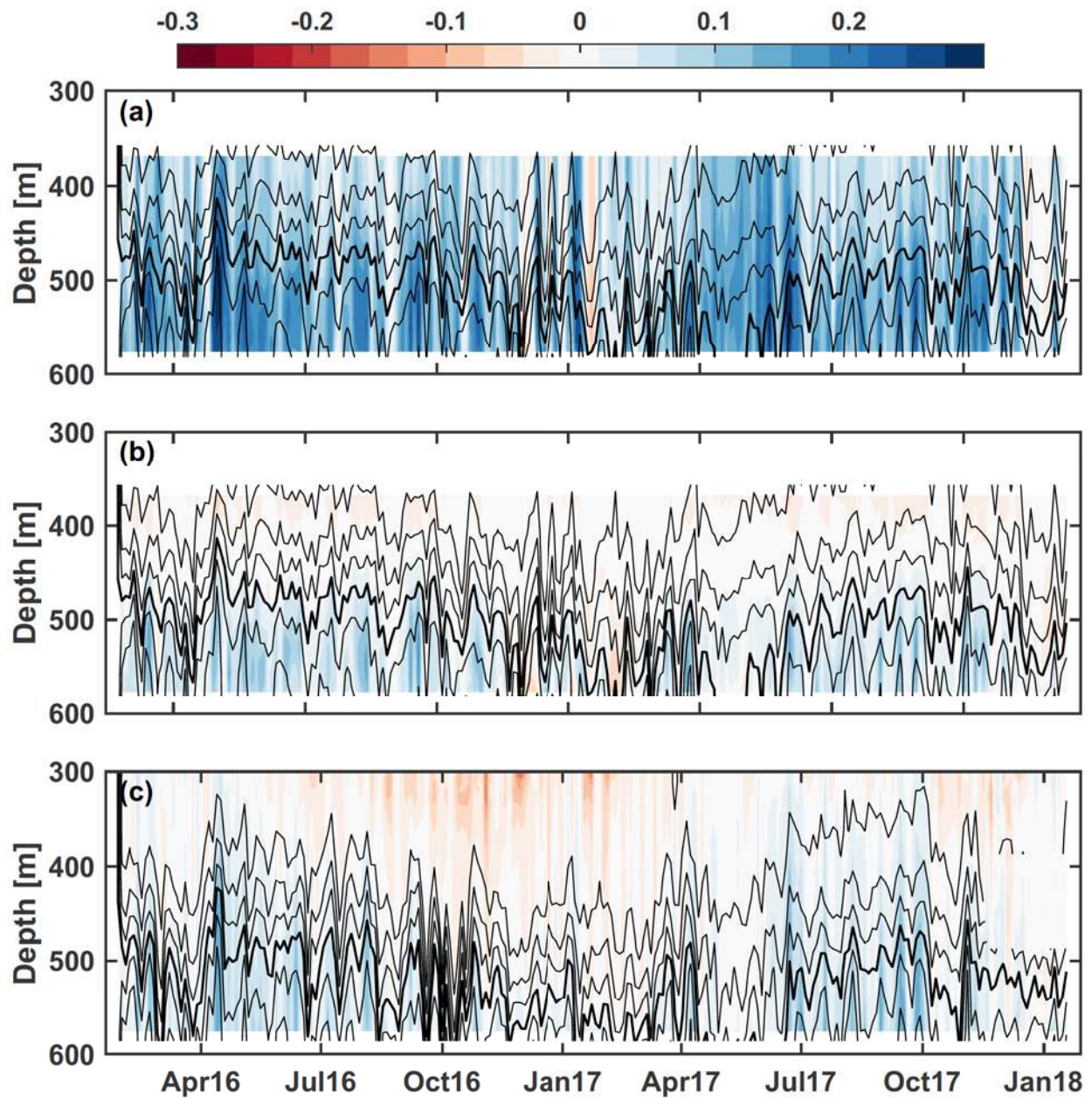
596 **Extended Data Figure 9. No blocking of depth-varying currents in laboratory.** Horizontal
597 velocities from the laboratory experiments are presented for the baroclinic flow with the three
598 different ice shelf configurations (Fig. 3b-d). Colors indicate velocity in the y-direction,
599 arrows indicate velocity vectors. (a)-(c) show velocities at the horizontal plane in the center of
600 the current (black lines in (d)-(i)), (d)-(f) show velocities at vertical sections underneath the
601 ice shelf (green lines in (a)-(c)) and (g)-(i) in front of it (magenta lines in (a)-(c)). Dashed and
602 shadowed rectangles indicate the ice shelf, grey shading indicates topography and grey lines
603 are bathymetric lines that the current is expected to follow. White areas are not measured/
604 missing data. The cyan arrow beneath the scale arrow in (a) - (c) indicate the temporal
605 standard deviation of the velocity and magenta bar indicates the error (Methods).

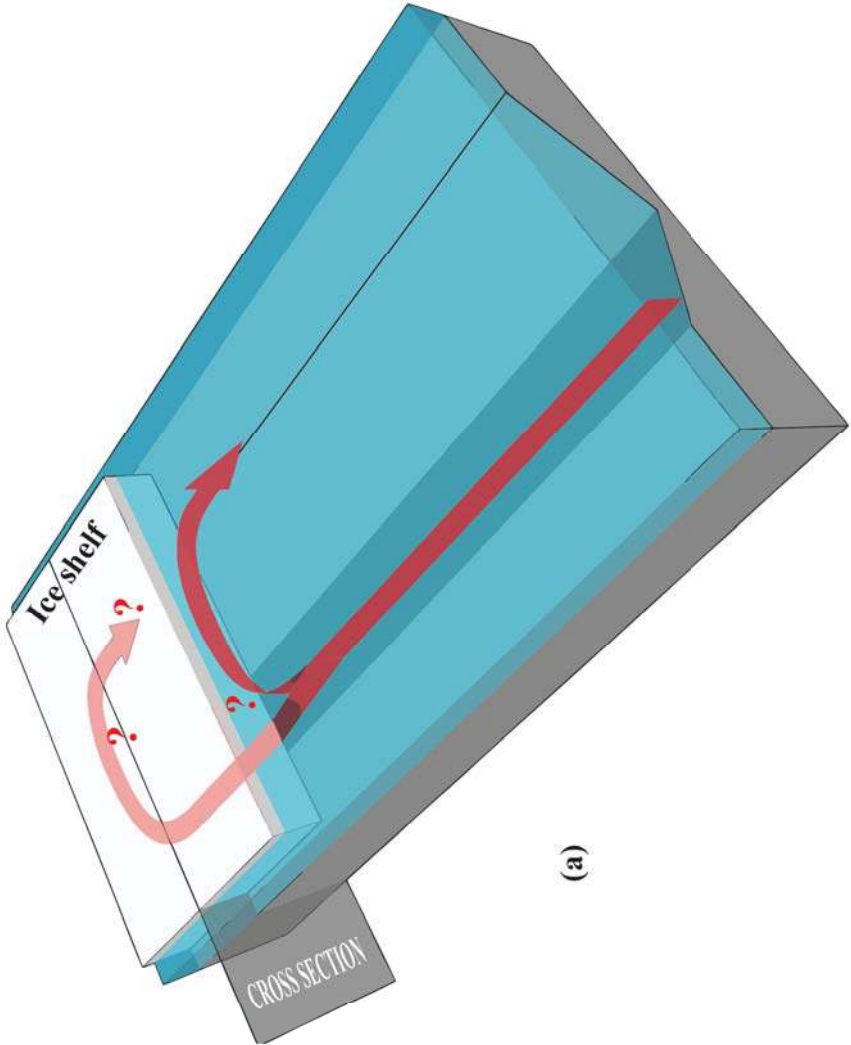
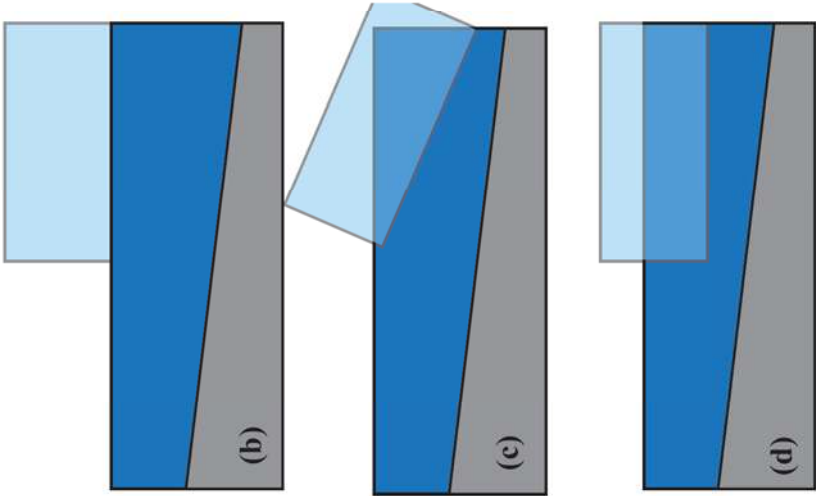
606 **Extended Data Table 1: Part of heat flux caused by the barotropic current component is**
607 **large compared to that caused by the baroclinic component.** Average heat flux (H) and its
608 barotropic (eq. (3)) and baroclinic (eq. (4)) components using different definitions of
609 barotropic velocity (i) Vertical average over the entire measured water column (ii) Vertical
610 average over the measured water column more than 150 m above the bottom (iii) Vertical
611 average over the measured water column above the -0.5° isotherm (see Methods). Also shown
612 is the part of the heat flux induced by the average velocity and temperature (\bar{H}) and their
613 fluctuating components (\tilde{H}) according to equation (6).

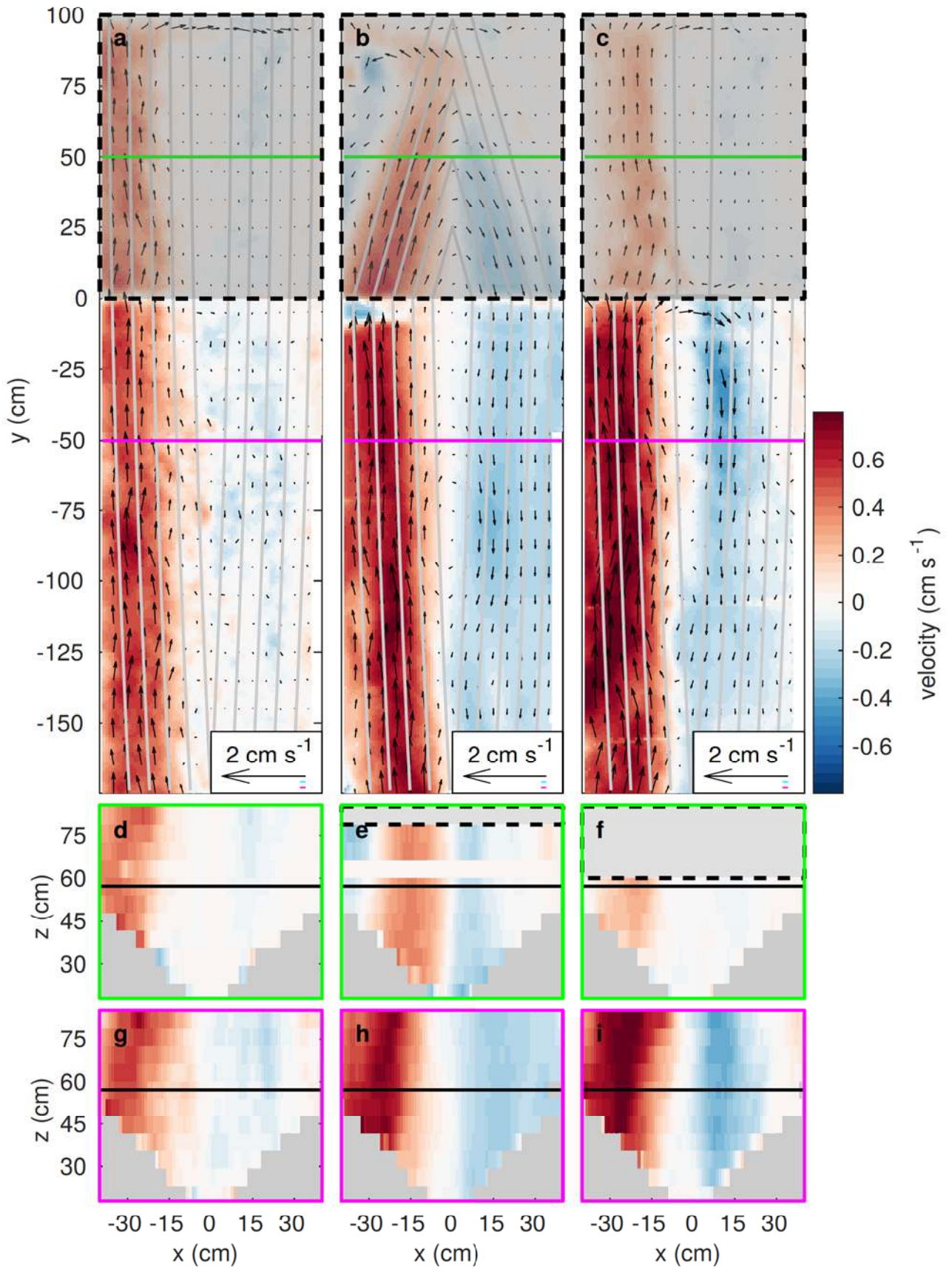
614 **Extended Data Table 2: Non-dimensional scales are similar in laboratory experiment**
615 **and observations.** Scale values for velocity (U), density difference ($\Delta\rho$), Coriolis parameter
616 (f), depth (H), width (L), molecular (in laboratory) or turbulent (in field) viscosity (ν) and the
617 derived Ekman depth (δ_E), Ekman number (Ek), Rossby radius (L_R) and Rossby number
618 (Ro). Observational parameters for velocity and density difference were obtained from the
619 GW1 and GW2 mooring data, while the bathymetric parameters were obtained from [31]. The
620 viscosity scale is a bulk eddy viscosity²².











Extended data

Extended Data Figure 1: Two year time series of velocity and temperature from GW1 mooring. Time series of (a) eastward velocity, (b) northward velocity and (c) temperature for the GW1 mooring. Black lines in (c) indicate positions of Microcats (thick lines) and SBE56 (thin lines).

Extended Data Figure 2: Two year time series of velocity and temperature from GW2 mooring. Time series of (a) eastward velocity, (b) northward velocity and (c) temperature for the GW2 mooring. Black lines in (c) indicate positions of Microcats (thick lines) and SBE56 (thin lines).

Extended Data Figure 3: Two year time series of velocity and temperature from GW3 mooring. Time series of (a) eastward velocity, (b) northward velocity and (c) temperature for the GW3 mooring. Black lines in (c) indicate positions of Microcats (thick lines) and SBE56 (thin lines).

Extended Data Figure 4: Comparison of methods for calculating barotropic component. Along-slope barotropic current component based on option (i): vertical average, option (ii): vertical average of the water more than 150 m above seabed, and option (iii): vertical average of water above the -0.5° isotherm according to legend. (a) Mooring GW1, 3-day averaged (b) Mooring GW2, 3-day averaged (c) Mooring GW3, 3-day averaged.

Extended Data Figure 5: The barotropic velocity is larger for GW1 and GW2 than GW3, the baroclinic velocity and the temperature increase towards the bottom. (a) Thick lines show average along-slope velocities as a function of distance above bottom, with colors indicating mooring (legend). Thin vertical lines show the barotropic components estimated according to method (i) (dotted lines), method (ii) (dashed lines), and method (iii) (solid lines). (b) Baroclinic velocity components as a function of distance above bottom. (c) Average temperature as a function of distance above bottom.

Extended Data Figure 6: The barotropic heat flux component is larger than the baroclinic for GW1 and GW2. Time series of total heat flux and the barotropic and baroclinic components using expression (2) and definition (ii) of barotropic velocity. (a) Mooring GW1 (b) Mooring GW2 (c) Mooring GW3.

Extended Data Figure 7. Experiment set-up and dimensions. (a) Top view drawing of v-shaped channel (blue), ice shelf (white), camera views (PCO1, green, PCO2, orange) and the source (to scale). (b) Side view drawing looking into the ice shelf facing South (c) Side view drawing looking East (d)-(f) Top views of topography (gray scale, color bar) and water column

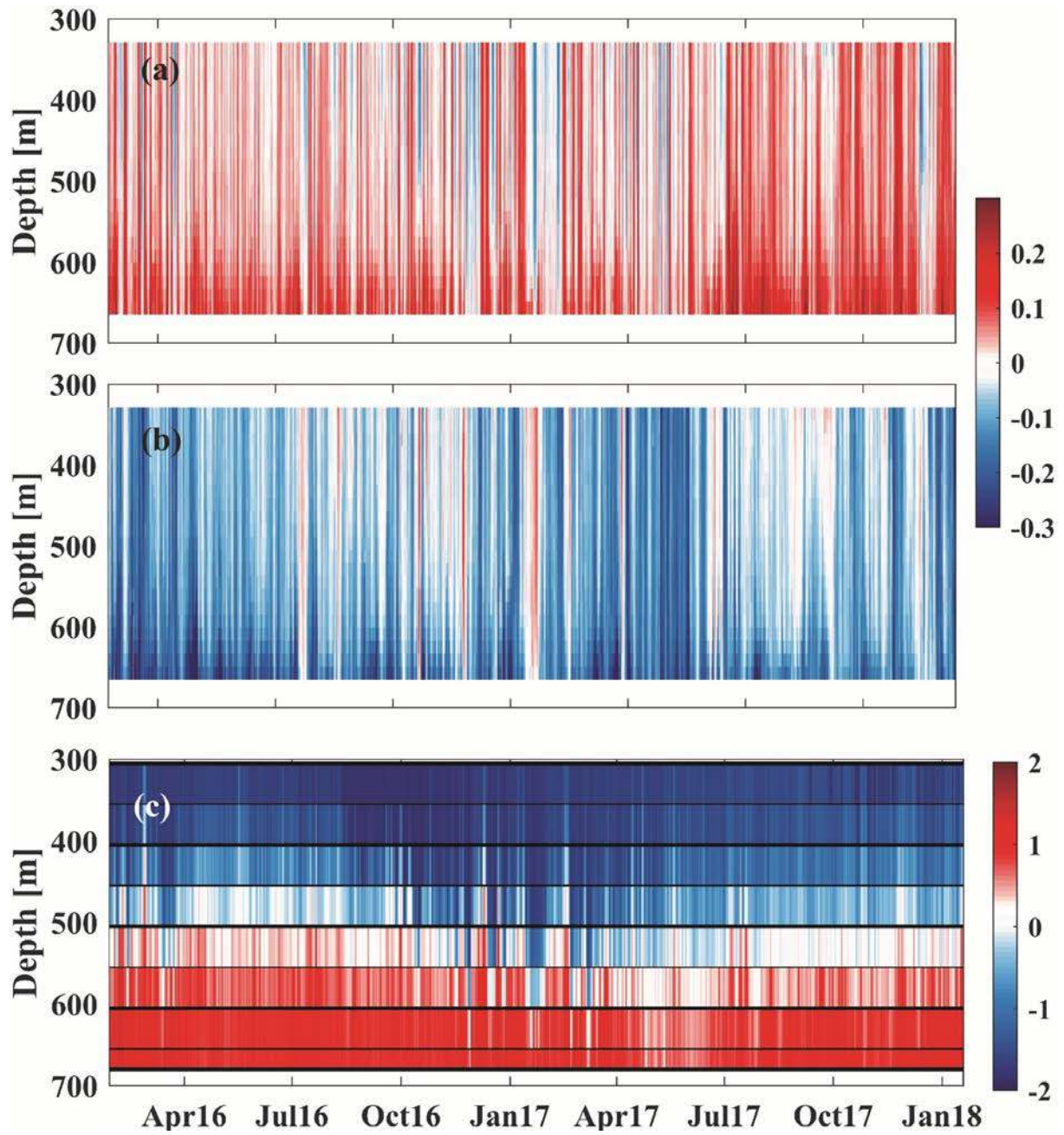
thickness (colored lines, labels) for (d) Ice shelf draft 0 cm (e) Ice shelf draft 30 cm, tilted (f) ice shelf draft 30 cm, horizontal.

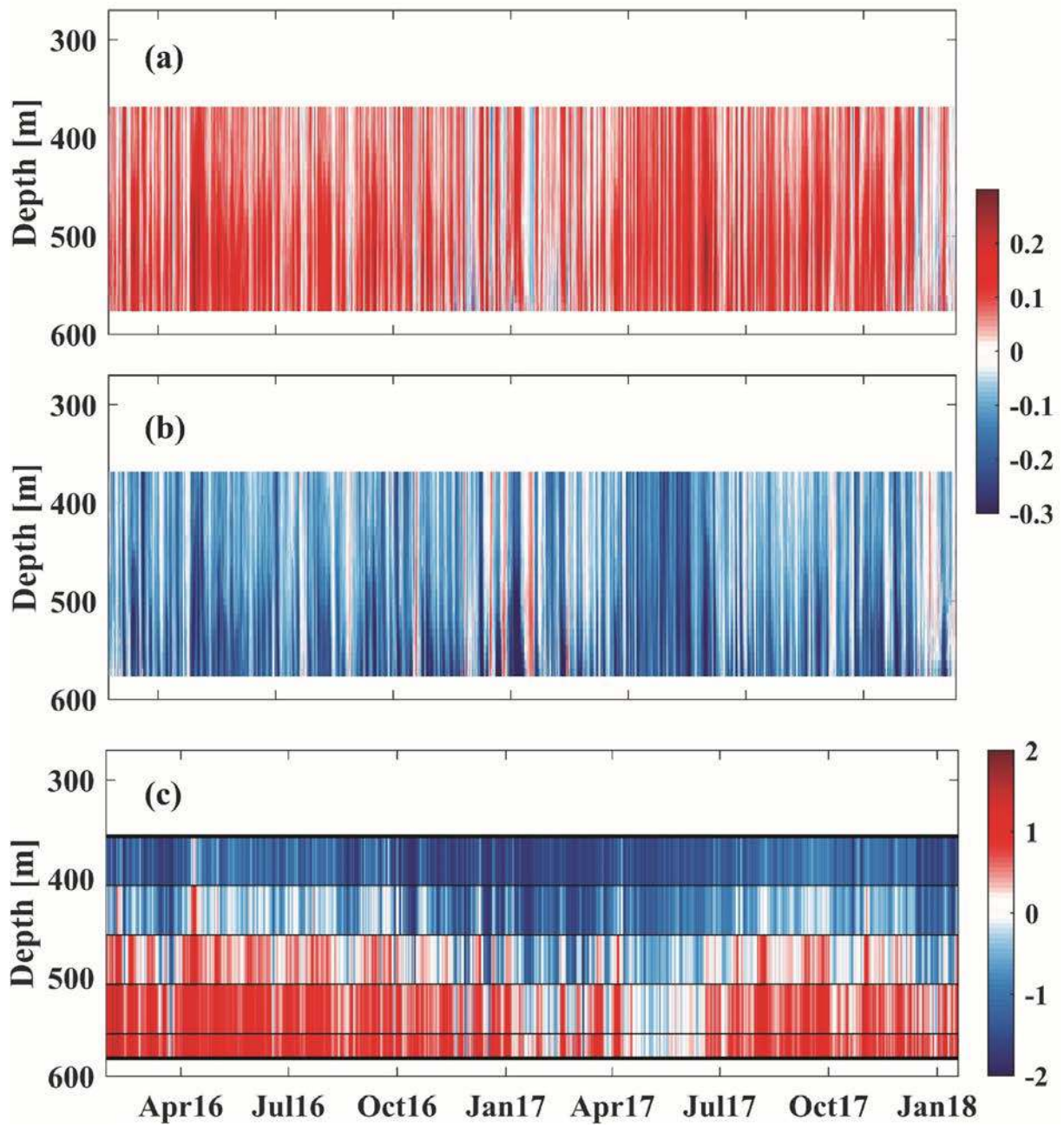
Extended Data Figure 8: Photographs from the experiments. (a) Top view showing the experimental set-up with the horizontal and vertical laser sheets. (b) Technicians and students preparing for an experiment (c) Time series showing the ice shelf cavity filling up with dense water for the baroclinic experiments (d) Top view photograph showing a barotropic current moving towards the ice shelf.

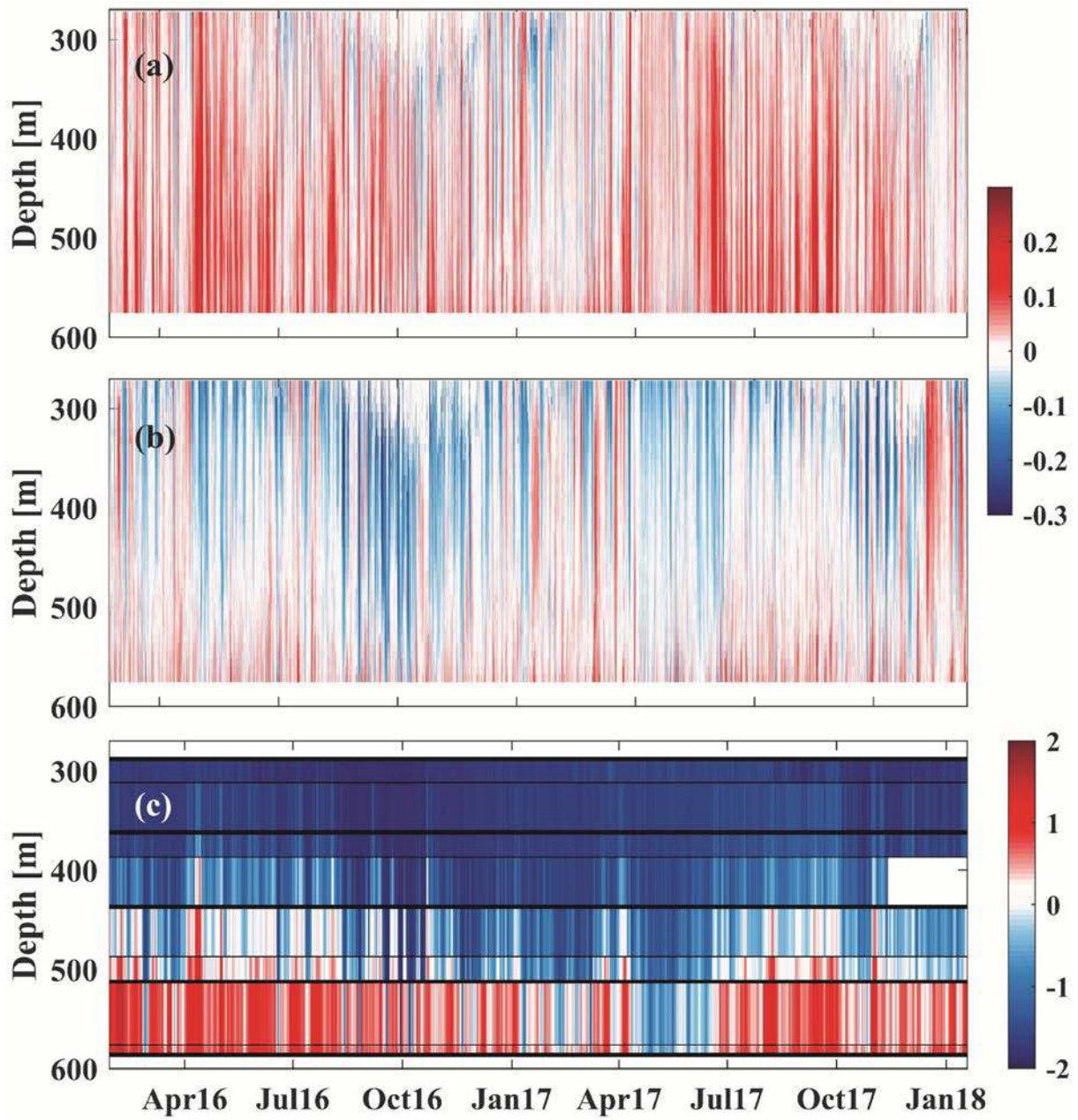
Extended Data Figure 9. No blocking of depth-varying currents in laboratory. Horizontal velocities from the laboratory experiments are presented for the baroclinic flow with the three different ice shelf configurations (Fig. 3b-d). Colors indicate velocity in the y-direction, arrows indicate velocity vectors. (a)-(c) show velocities at the horizontal plane in the center of the current (black lines in (d)-(i)), (d)-(f) show velocities at vertical sections underneath the ice shelf (green lines in (a)-(c)) and (g)-(i) in front of it (magenta lines in (a)-(c)). Dashed and shadowed rectangles indicate the ice shelf, grey shading indicates topography and grey lines are bathymetric lines that the current is expected to follow. White areas are not measured/missing data. The cyan arrow beneath the scale arrow in (a) - (c) indicate the temporal standard deviation of the velocity and magenta bar indicates the error (Methods).

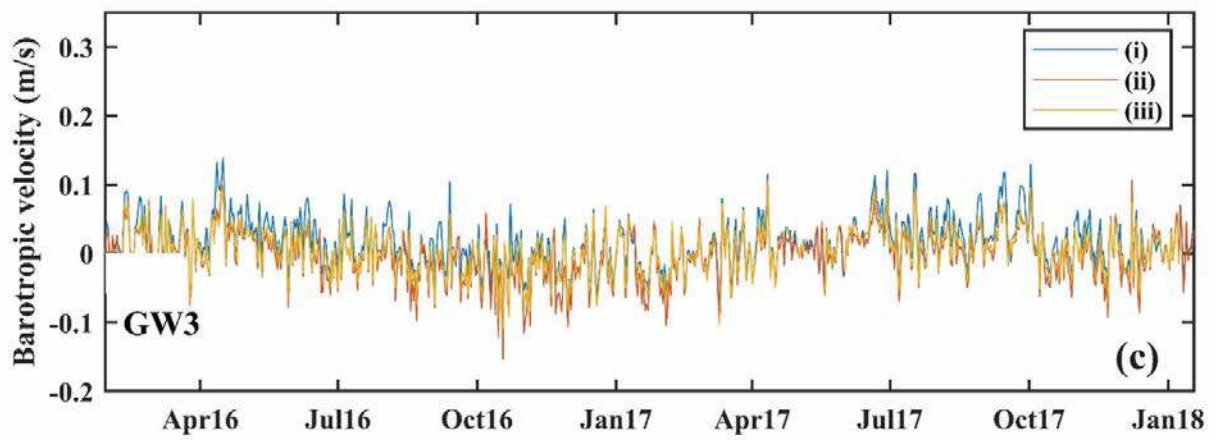
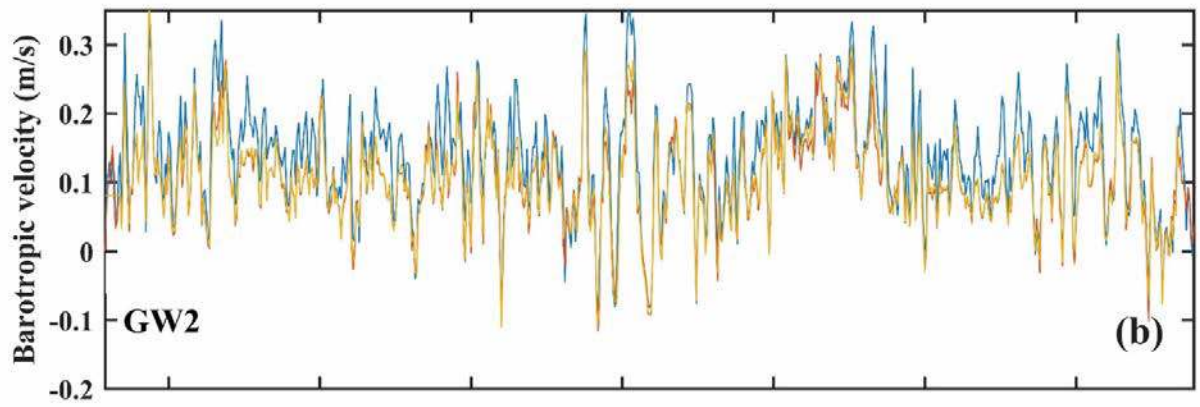
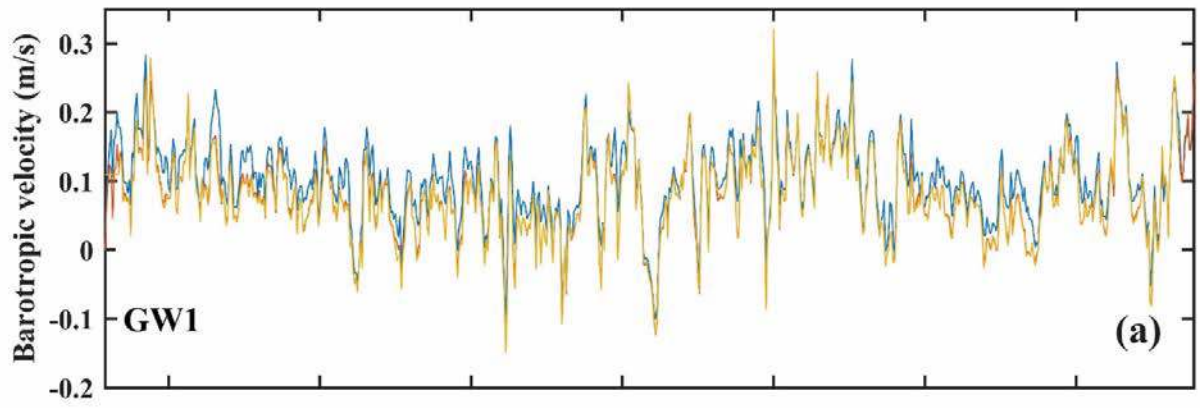
Extended Data Table 1: Part of heat flux caused by the barotropic current component is large compared to that caused by the baroclinic component. Average heat flux (H) and its barotropic (eq. (3)) and baroclinic (eq. (4)) components using different definitions of barotropic velocity (i) Vertical average over the entire measured water column (ii) Vertical average over the measured water column more than 150 m above the bottom (iii) Vertical average over the measured water column above the -0.5° isotherm (see Methods). Also shown is the part of the heat flux induced by the average velocity and temperature (\overline{H}) and their fluctuating components (\tilde{H}) according to equation (6).

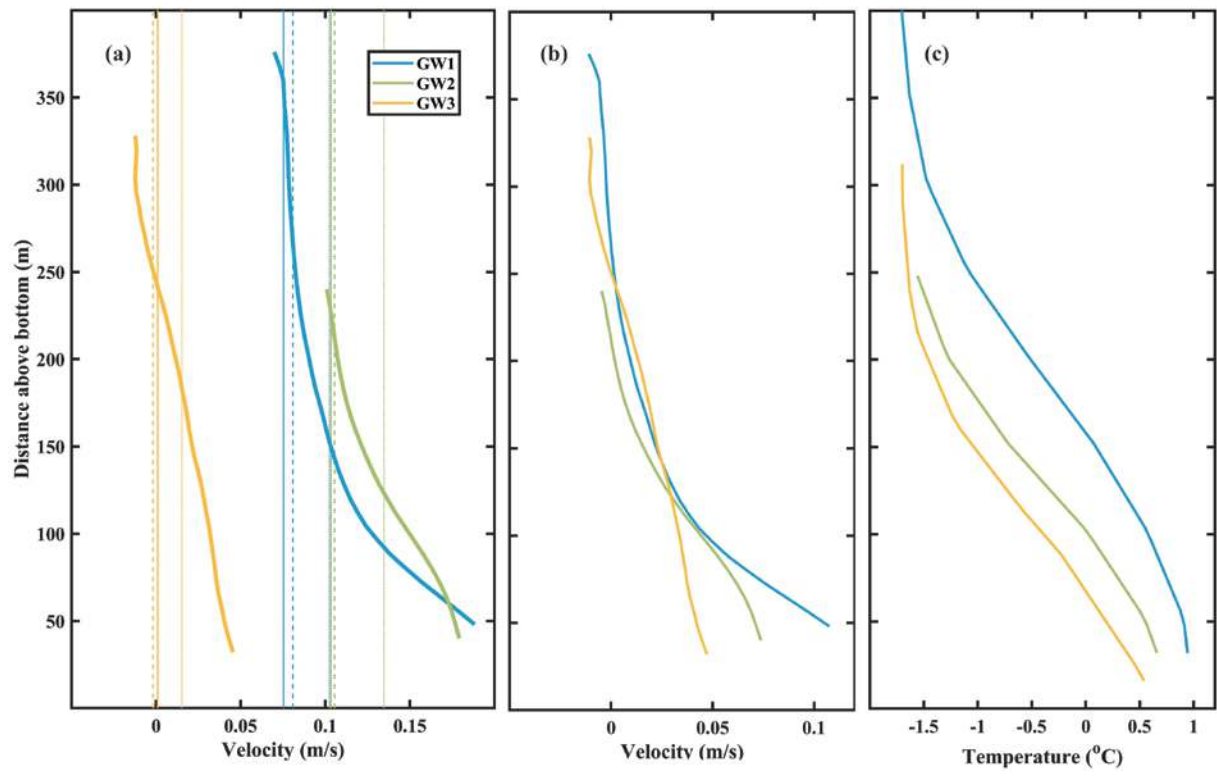
Extended Data Table 2: Non-dimensional scales are similar in laboratory experiment and observations. Scale values for velocity (U), density difference ($\Delta\rho$), Coriolis parameter (f), depth (H), width (L), molecular (in laboratory) or turbulent (in field) viscosity (ν) and the derived Ekman depth (δ_E), Ekman number (Ek), Rossby radius (L_R) and Rossby number (Ro). Observational parameters for velocity and density difference were obtained from the GW1 and GW2 mooring data, while the bathymetric parameters were obtained from [31]. The viscosity scale is a bulk eddy viscosity²².

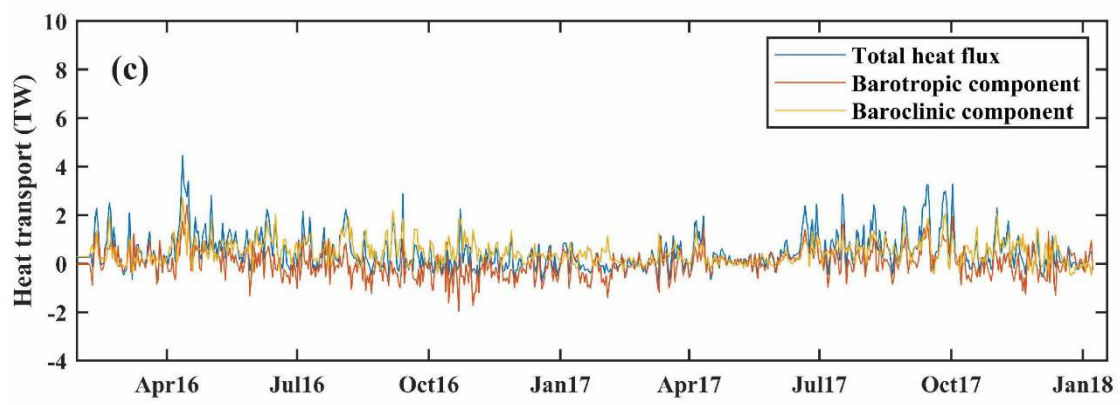
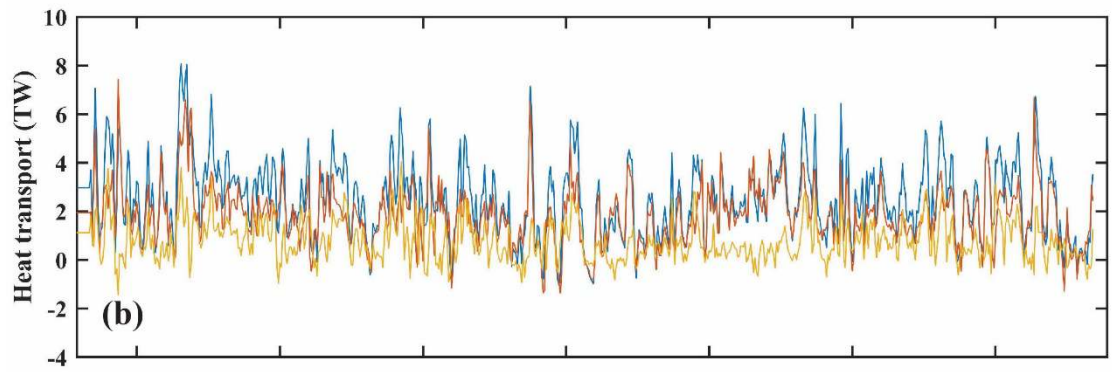
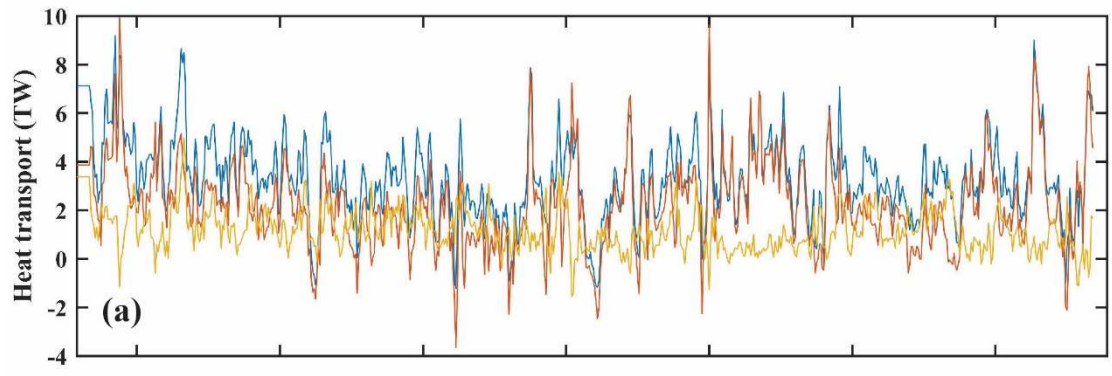


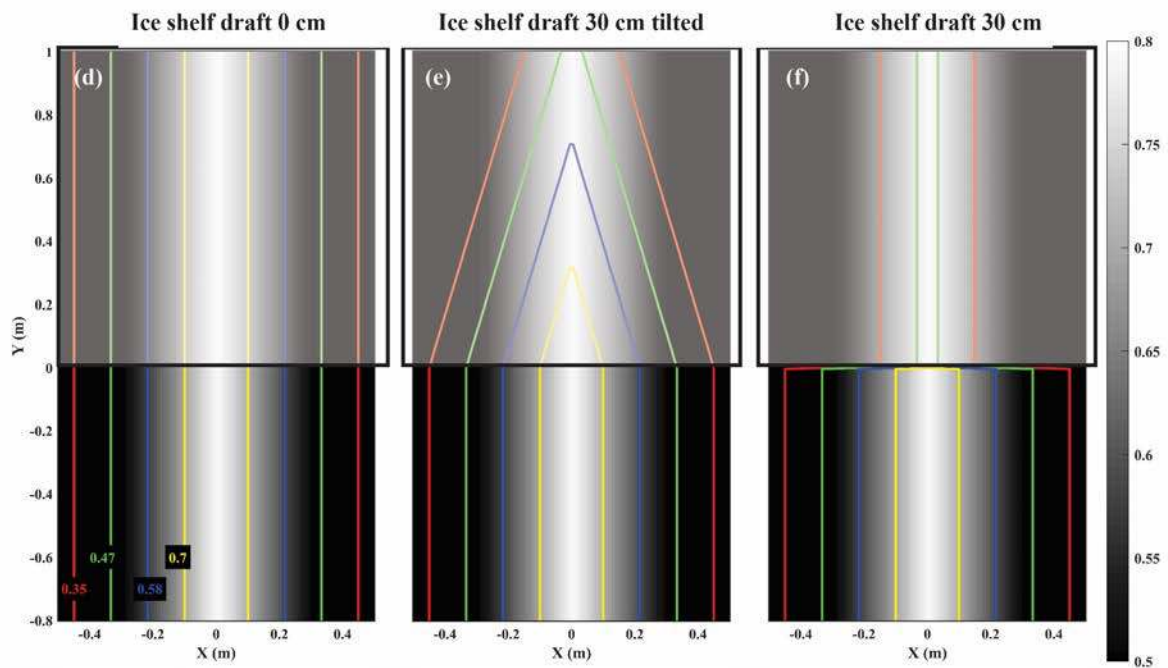
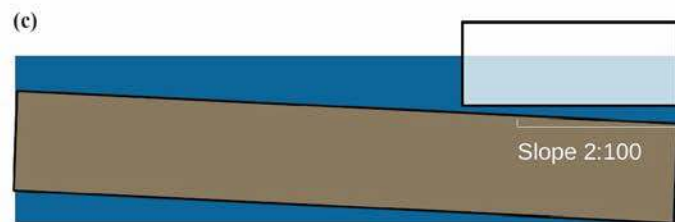
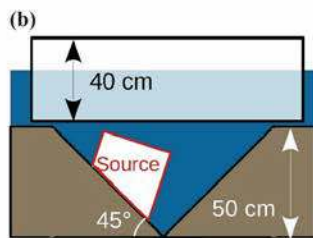
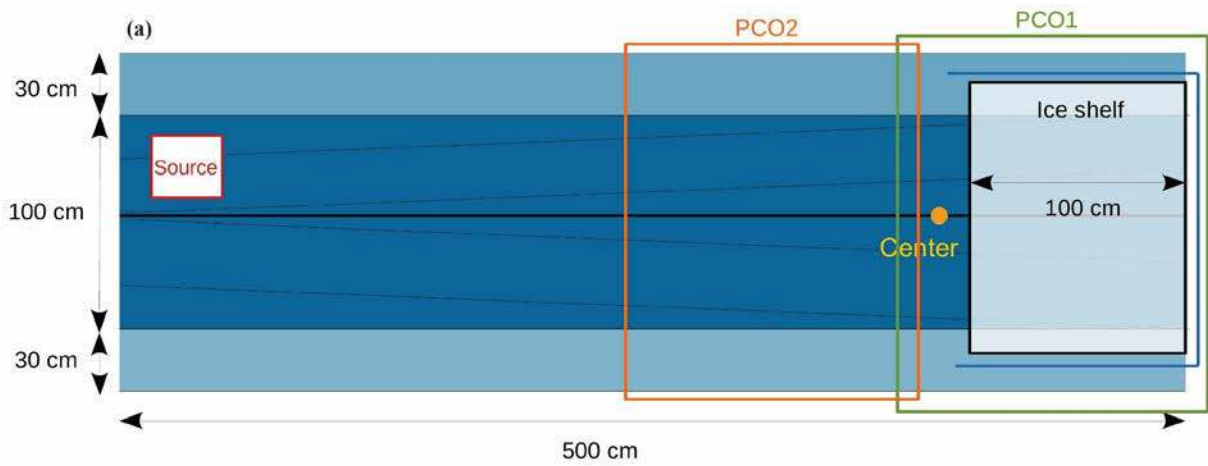


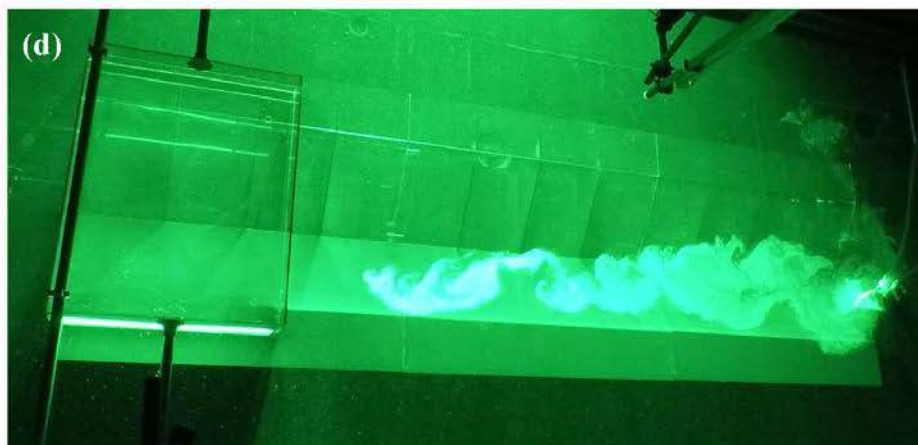
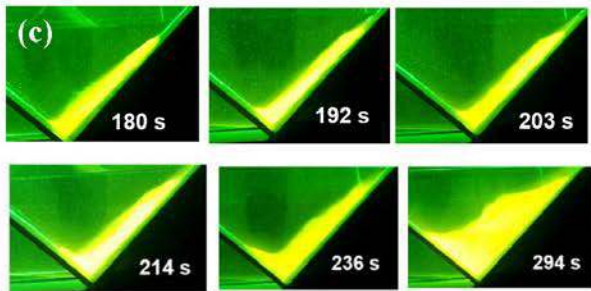
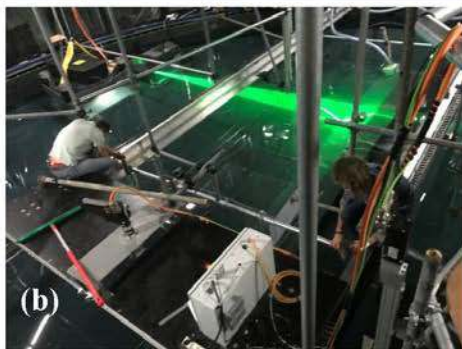
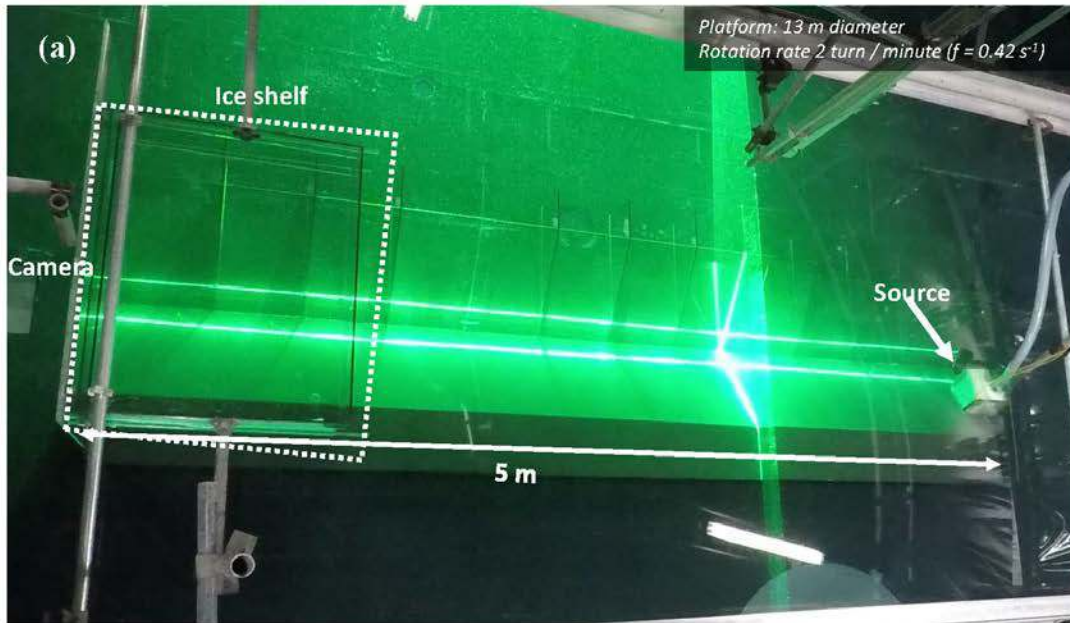


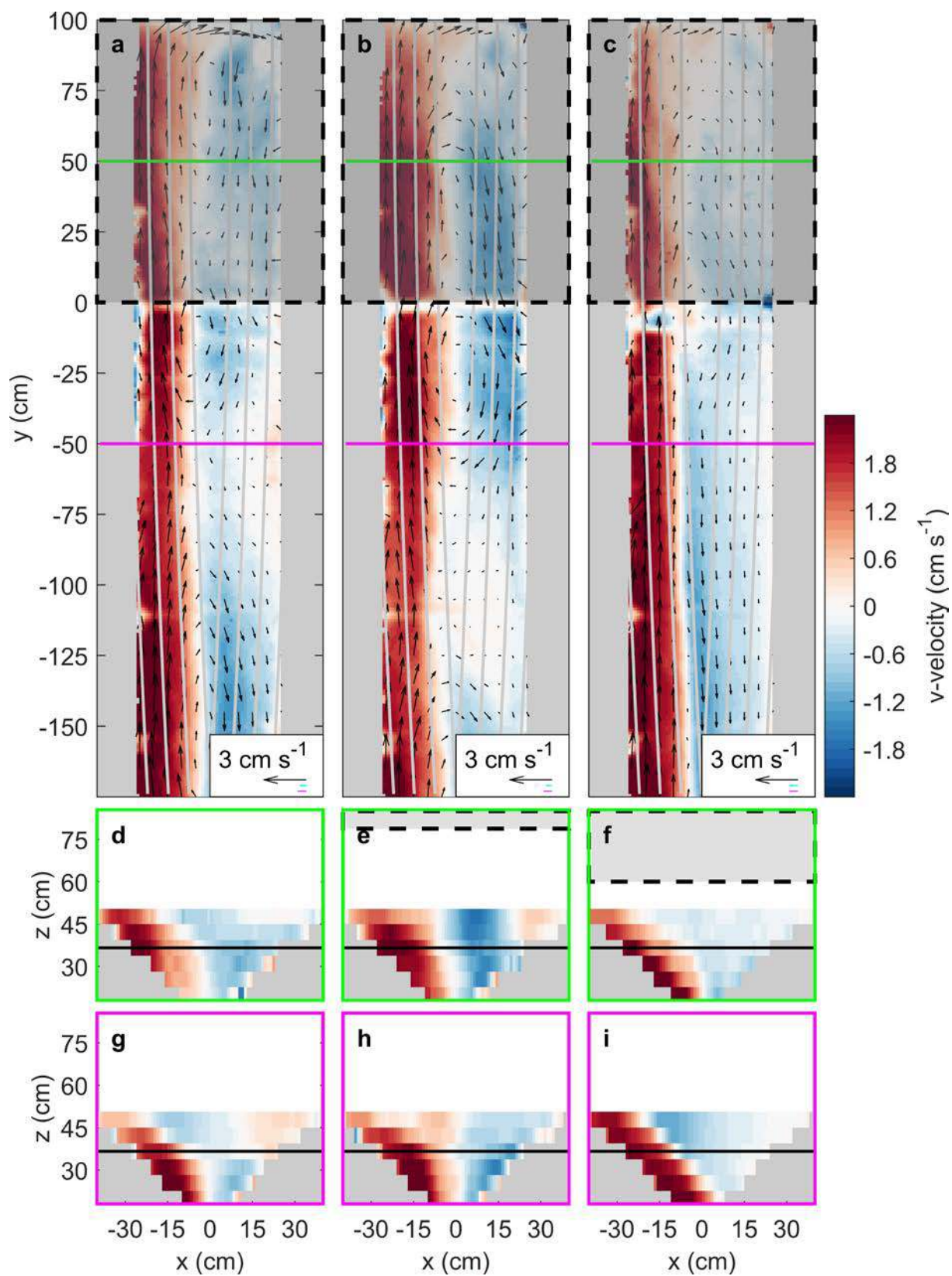












Extended Data Table 1: Part of heat flux caused by the barotropic current component is large compared to that caused by the baroclinic component.

	GW1	GW2	GW3
\mathbf{H}	2.8 TW	2.27 TW	0.47 TW
$\overline{\mathbf{H}}$	2.64 TW (94%)	2.14 TW (94%)	0.38 TW (80%)
$\tilde{\mathbf{H}}$	0.16 TW (6%)	0.13 TW (6%)	0.09 TW (20%)
\mathbf{H}_{BT} (method (i))	2.49 TW (89%)	2.11 TW (93%)	0.28 TW (60%)
\mathbf{H}_{BC} (method (i))	0.31 TW (11%)	0.16 TW (7%)	0.19 TW (40%)
\mathbf{H}_{BT} (method (ii))	1.96 TW (70%)	1.61 TW (71%)	0.01 TW (3%)
\mathbf{H}_{BC} (method (ii))	0.84 TW (30%)	0.66 TW (29%)	0.46 TW (97%)
\mathbf{H}_{BT} (method (iii))	1.88 TW (67%)	1.59 TW (70%)	0.05 TW (10%)
\mathbf{H}_{BC} (method (iii))	0.92 TW (33%)	0.68 TW (30%)	0.42 TW (90%)

Extended Data Table 2: Non-dimensional scales are similar in laboratory experiment and observations.

Symbol [unit]	Laboratory	Observations	Description
\mathbf{U} [m s^{-1}]	0.03	0.2	Velocity
$\Delta\rho$ [kg m^{-3}]	2	0.3	Density difference
\mathbf{f} [s^{-1}]	0.42	10^{-4}	Coriolis parameter
\mathbf{H} [m]	0.5	500	Depth
\mathbf{L} [m]	0.5	10^4	Width
\mathbf{v} [$\text{m}^2 \text{s}^{-1}$]	10^{-6}	10^{-4}	Viscosity
$\delta_E = \sqrt{\nu/f}$ [m]	0.0015	1	Ekman depth
$\mathbf{Ek} = \delta_E^2/H^2$	$0.9 \cdot 10^{-5}$	$0.4 \cdot 10^{-5}$	Ekman number
$\mathbf{L}_R = U/f$ [m]	0.07	2000	Rossby radius
$\mathbf{Ro} = L_R/L$	0.14	0.2	Rossby number